

# **Landmark Detection in Retinal Images**

Thesis submitted in partial fulfillment  
of the requirements for the degree of

MS in Electronics and Communication Engineering by Research

by

Gaurav Mittal

201232644

`gaurav.mittal@research.iiit.ac.in`



International Institute of Information Technology

Hyderabad - 500 032, INDIA

June 2018

Copyright © Gaurav Mittal, 2018  
All Rights Reserved

International Institute of Information Technology  
Hyderabad, India

**CERTIFICATE**

It is certified that the work contained in this thesis, titled “Landmark Detection in Retinal Images” by Gaurav Mittal, has been carried out under my supervision and is not submitted elsewhere for a degree.

---

Date

---

Adviser: Prof. Jayanthi Sivaswamy

To friends and family

## **Acknowledgments**

First and foremost, I would like to express my sincere gratitude to my advisor Prof. Jayanthi Sivaswamy for her continuous support and guidance. She taught me to see the bigger picture, guided me when I failed and helped me develop a healthy attitude towards research. I hope to put the things that she has taught me to good use in the future.

I would also like to thank my batch mates and MS2K12 batch for making the stay at IIIT memorable and fun. I thank my lab mates in CVIT for being a part of the interactive work environment. I would like to thank all my friends who have always been there for me in good and bad times alike.

Last but not the least, I would like to thank my parents, my sister and my grandparents for all their love and support. Their belief in me has always helped me sail through the tough times.

## Abstract

Advances in medical field and imaging systems have resulted in a series of devices that sense, record, transform and process digital data. In the case of human eyes this digital data is fundus images, which are images of the back part of our retina. Automatic analysis of these images is required to process large amount of data and help doctors make the final diagnosis. Retina images has 3 major visible landmarks: Optic disk(OD), macula and blood vessels. In retina images, OD appears as a bright elliptical structure, macula appear as a small dark region and blood vessel appears as dark tree branch like structure. In this thesis, we have proposed methods for detection of retina landmarks.

Accurate detection of OD and macula is important as computer assisted diagnosis systems uses location of these landmarks for understanding the retina image and using clinical facts about retina for improving diagnosis. Retina landmark detection also aids in assessing the severity of diseases based on the locations of abnormalities relative to these landmarks. We first used retina atlas for OD and macula detection. The idea of retina atlas is inspired by brain 3D atlas [34]. We create 2 retina atlases: intensity atlas and probability atlas, by annotating public datasets locally. We use probabilistic atlas for OD and macula detection but detection rates and accuracy of the system is low. To achieve better detection, we than used Generalized motion patterns(GMP) [14][23] for OD and macula detection. The GMP is derived by inducing motion to an image, which serves to smooth out unwanted information while highlighting the structures of interest. Our GMP based detection is fully unsupervised and its results outperformed all other unsupervised methods. The results are comparable to that of supervised methods. The proposed GMP based system is completely parallelizable and handles illumination differences efficiently.

Blood vessels are another important retina landmark and we find that the current research uses evaluation measure like sensitivity, specificity, accuracy, area under curve and matthew correlation coefficient for evaluating vessel segmentation performance. We find several gaps in current evaluation measures and propose local accuracy, which is an extension of [39]. We show that local accuracy is especially useful in settings, where segmentation of weak vessels and accurate estimation of vessel width is required.

# Contents

Chapter	Page
1 Introduction . . . . .	1
1.1 The Human Retina . . . . .	1
1.2 Motivation for automated analysis and landmark detection . . . . .	3
1.3 Thesis focus and contributions . . . . .	4
1.4 Organization of this thesis . . . . .	4
2 Optic disk and macula detection using Retina Atlas . . . . .	6
2.1 Introduction . . . . .	6
2.2 Data marking . . . . .	7
2.3 Retina atlas generation . . . . .	10
2.3.1 Intensity atlas generation . . . . .	10
2.3.2 Probability atlas generation . . . . .	12
2.4 OD and macula detection using probability atlas . . . . .	13
2.4.1 OD detection . . . . .	14
2.4.2 Macula detection . . . . .	15
2.4.3 Vessel arcade detection . . . . .	16
2.4.4 Joint OD macula registration . . . . .	16
2.4.5 Experimental results . . . . .	17
2.5 Summary . . . . .	19
3 Optic disk and macula detection using Generalized Motion pattern . . . . .	20
3.1 Introduction . . . . .	20
3.2 GMP and interference map . . . . .	21
3.3 Optic disk detection using interference map . . . . .	24
3.3.1 Optic disk candidate selection . . . . .	24
3.3.2 Determining the final optic disk location . . . . .	24
3.4 Macula detection using detected optic disk . . . . .	27
3.5 Results and Experiments . . . . .	28
3.6 Summary . . . . .	31
4 An effective metric for evaluating retina blood vessel segmentation performance: Local accuracy	32
4.1 Introduction . . . . .	32
4.2 Related works . . . . .	33
4.3 Local accuracy . . . . .	34
4.4 Results and experiments . . . . .	37

4.4.1	Discriminative power . . . . .	37
4.4.2	Effect of change in FOV . . . . .	37
4.4.3	Penalizing mis-detection due to lesions and other abnormalities . . . . .	38
4.4.4	Local accuracy as an optimization method . . . . .	39
4.5	Summary . . . . .	42
5	Conclusions . . . . .	43
	Bibliography . . . . .	45

## List of Figures

Figure	Page
1.1 Right human eye cross-sectional view. Source: <a href="https://en.wikipedia.org/wiki/Retina">https://en.wikipedia.org/wiki/Retina</a> . . .	2
1.2 General setup in Fundus photography. Source: Retina wiki page. . . . .	2
1.3 Sample retina images of a normal and an abnormal eye in left and right positions respectively. . . . .	3
2.1 Tool for marking OD, macula and vessel arcades. . . . .	8
2.2 Left and center image: Skipped images because of non-visible macula. Right image: Skipped image because of non-definitive upper vessel arcade. . . . .	9
2.3 Marked data shown for a sample left eye retina image (cropped for viewing purposes) .	9
2.4 Point-sets for TPS registration. Points taken are OD, macula and equidistant points in vessel arcades. . . . .	10
2.5 Chosen left and right eye base images for creating intensity atlas (For Messidor dataset [35]). . . . .	11
2.6 Intensity atlas for Left and right eye images (For first 400 Messidor images). . . . .	11
2.7 Left and right eye intensity atlas for first 400 Messidor images. Here arcades are represented by parabola and equidistant points are taken on parabola. . . . .	12
2.8 Vessel arcade sampling for vessel probability atlas generation. . . . .	14
2.9 Probability retina atlas for left and right eye. Red, blue and green channel represents OD, macula and arcade probability atlases respectively. . . . .	15
2.10 Left to right: Sample retina image, OD feature map, macula feature map. . . . .	15
2.11 From left to right: Sample image, vesselness image using [25], Detected vessel arcades.	16
2.12 Overview of our work. . . . .	17
2.13 Output of the algorithm on sample images from messidor [35]. OD is marked as black dot and macula is marked as black cross. . . . .	18
3.1 From left to right: Original image, min GMP and max GMP interference map. In these maps, coalescing function $f(\cdot)$ is max/min and $\phi(\cdot)$ is mean. These interference maps are normalized for viewing purposes. . . . .	22
3.2 GMP and interference map for samples images from Directdb (top row) and Messidor (bottom row). From left to right: original image, GMP about the pivot shown as white cross and interference map. . . . .	23
3.3 max and median interference map for samples images from Messidor (top row) and Directdb (bottom row). From left to right: Original image, max interference map with $f(\cdot)$ as max and $\phi(\cdot)$ as mean and median interference map with $f(\cdot)$ as median and $\phi(\cdot)$ as quartile point generator. . . . .	23

3.4	Example GMP interface map and respective binary maps. Binary maps are shown only for rectangular area marked by white lines in interference image. . . . .	25
3.5	Example image and respective vesselness and horizontal gradient image. . . . .	26
3.6	Example image and respective interference map with candidate points shown as white dots. Pink, yellow and blue squares represents rejection because of stage 1,2,3 respectively. Final detected OD is surrounded by green square. . . . .	27
3.7	Overview of over system. . . . .	28
3.8	OD and macula detection results (Black cross represents OD and white cross represents macula). Top two rows show correct detections in images from Messidor and DMED, respectively. Last row shows failure cases (from left to right) due to image capture, failure in rejection stages and presence of large pathologies. . . . .	29
4.1	From left to right a) Original image b) Segmented vessels using [31] c) Manually marked vessels d) Neighborhood pixels . . . . .	36
4.2	From left to right a) Original image b) Manually marked vessels c) Segmented vessels using [25] d) Segmented vessels using [28]. . . . .	37
4.3	From left to right a) Drive image b) Stare image . . . . .	38
4.4	From left to right a) Original image b) Manually marked vessels c) Segmented using [39] and optimized for accuracy d) Optimized for Local accuracy. . . . .	41

## List of Tables

Table	Page
2.1 Marking statistics for public datasets. . . . .	9
2.2 Comparison of OD detection rates on popular datasets . . . . .	18
2.3 Comparison of detection rates for macula on popular datasets . . . . .	18
3.1 Results for Optic disk detection . . . . .	29
3.2 Comparison of Detection Rates for OD . . . . .	30
3.3 Detection rates for macula on popular datasets . . . . .	30
4.1 Accuracies and local accuracies for Drive [13] dataset. Threshold optimized for maximizing accuracy. . . . .	40
4.2 Accuracies and local accuracies for Drive [13] dataset. Threshold optimized for maximizing local accuracy. . . . .	40
4.3 Accuracies and local accuracies for Stare [26] dataset. Threshold optimized for maximizing accuracy. . . . .	41
4.4 Accuracies and local accuracies for Stare [26] dataset. Threshold optimized for maximizing local accuracy. . . . .	42
4.5 Comparison of different evaluation metrics. . . . .	42

## *Chapter 1*

### **Introduction**

#### **1.1 The Human Retina**

Retina is the light sensitive layer of tissue which captures the image of the visual world much like the film in a camera. The black visible circle in the center of our eyes is called pupil and at its center there is a small hole present called iris. Light passes through iris, which forms an image of the scene on retina by initiating a cascade of chemical and electric events. These event signals are sent to various centers of brain through the optic nerves. The brain finally understands these signals and the image is formed in our mind. Fig. 1.1 shows the cross-sectional view of human eye for explaining the eye anatomy.

Digital images of retina are captured using 2 techniques: fundus photography and Optical Coherence Tomography(OCT). OCT imaging is similar to ultrasound but it uses light rather than sound waves to achieve higher resolution pictures of the structural layers of the back of the eye. In this work, we have only worked with images captured using fundus photography.

Fundus photography involves capturing the image of the back part of the eye i.e. retina tissue layer which captures the light. This retina tissue is also called fundus of the eye and these terms are interchangeable. From now on we will refer to the images of retina tissue layer as retina images. Pupil is generally dilated(enlarged) before capturing the retina images (of fundus tissue). This allow more light to pass through iris and results in retina images with higher SNR.

Specialized fundus cameras, which consist of an intricate microscope attached to a flashed enabled camera is used to photograph retina. Flash in the camera works as the light source and the light is projected through the dilated pupil onto the retina tissue layer. The lenses focus on retina so that the observer can look at the retina and finally CCD camera is used to capture the retina image. Fig. 1.2 shows an image of general setup and Fig. 1.3 shows some examples of retina images. The main structures that can be visualized on a retina image are optic disc, macula and blood vessels. Optic disk, macula and blood vessels are important landmarks in retina images.

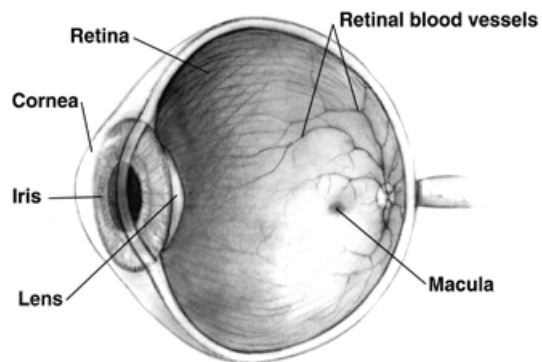


Figure 1.1: Right human eye cross-sectional view. Source: <https://en.wikipedia.org/wiki/Retina>



Figure 1.2: General setup in Fundus photography. Source: Retina wiki page.

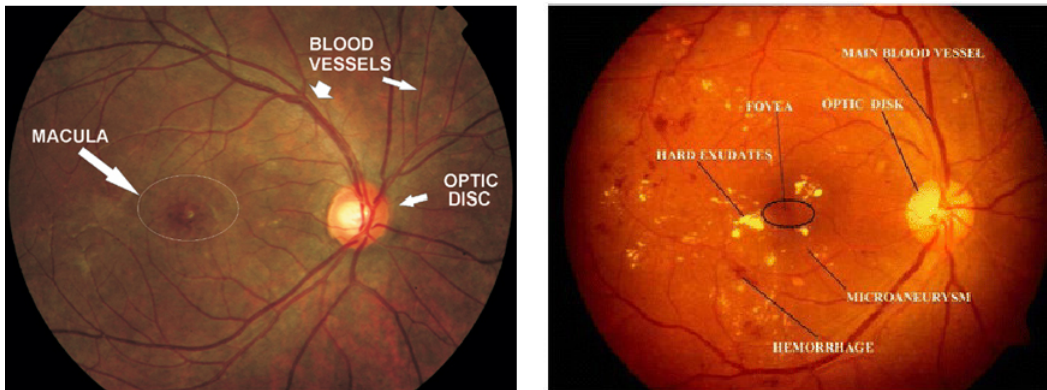


Figure 1.3: Sample retina images of a normal and an abnormal eye in left and right positions respectively.

## 1.2 Motivation for automated analysis and landmark detection

Early diagnosis and timely treatment can prevent up to 98% of severe vision loss in sight threatening diseases like Diabetic retinopathy and Glaucoma etc. Digital images of the retina is used for screening such diseases and their automated analysis is crucial to handle large scale of data.

Retina diseases like Hypertensive retinopathy is associated with systemic arterial hypertension. A patient with undiagnosed hypertension will probably consult an ophthalmologist first with a complaint of visual loss, which place ophthalmologists in a unique position to detect the hypertension disease and prevent vision loss because of this. Hypertension is ranked as one of the top 10 risk factors for burden of diseases in developed countries by the World Health Organization. Due to modern lifestyle and high stress work culture, it is very likely that more patients will have hypertension and vision loss in near future.

Another disease, Diabetic retinopathy has even more concerning situation. Diabetes is a growing disease in the world which is due to population growth, aging, urbanization and increasing prevalence of obesity and physical inactivity. Population with diabetes as of today is estimated to be around 200 millions of people worldwide. It is estimated to grow by the 37 percent by 2030. Diabetic retinopathy is the result of diabetes and since large population has diabetes, diabetic retinopathy is the most common cause of blindness. In the United States, it is the first cause of blindness in working age population. The underlying cause of blindness in most diabetic patients is mis-diagnosis and late discovery of disease and not the disease itself.

Solid infrastructure and automated analysis is required to diagnose and treat these diseases and control blindness. The current approach of retina disease diagnosis is direct examination by an ophthalmologist. An automated system to analyze the retinal images and make diagnosis can be really useful for ophthalmologists and medical examiners. Such system can improve efficiency and speed of diagnosis, while lowering down diagnosis cost. It can help ophthalmologists by suggesting diagnosis and making

automatic diagnosis in clear cases. Since the number of ophthalmologists available is limited and a large population is at the risk of serious diseases; such automated systems are need of the hour. Recent development in digital imaging and computing allows impressive capabilities of storage, transfer, and quantization of retinal images. This makes research, development and testing of automated analysis algorithm efficient and fast.

Retina research community has done significant work in developing algorithms and methods for analysis of retina images and diagnosis of retina diseases. Most of these efforts has been in developing diseases specific diagnosis systems for diseases like Diabetic Retinopathy, Retinopathy of Prematurity etc. These disease specific diagnosis systems need the location of Optic disk and macula for image alignment, image registration, atlas creation etc. The accurate location of optic disk and macula also helps in utilizing the clinical facts about retina to improve detection performance. For example, the OD location can be used to boost the bright lesion detection performance of Computer assisted diagnosis(CAD) algorithms, as OD share many visual characteristics with bright lesions. The location of OD and macula also aids in determining the severity of the disease and need for intervention. Improvements in Optic disk and macula detection accuracy benefits the whole field as most methods needs to detect Optic disk and macula for image understanding. The performance of automated diagnosis system is directly proportional to the accuracy of Optic disk and macula detection systems.

### **1.3 Thesis focus and contributions**

The aim of the thesis is to propose and facilitate the landmark detection methods in retina images. In this thesis, we propose methods for detection of Optic disk and macula using atlas and Generalized motion patterns (GMP). We also propose a new evaluation measure to analyze vessel segmentation performance. The key contributions of the thesis are

1. Exploring the use of atlas in retina images and proposal of probabilistic and intensity atlas.
2. Modifying Generalized motion pattern (GMP) to suit Optic disk and macula detection problem.
3. Using modified GMP to propose a fully unsupervised Optic disk and macula detection algorithm with better performance compared to other unsupervised works.
4. Finding some gaps in existing vessel segmentation evaluation measures and proposing local accuracy. Local accuracy is much more suitable evaluation metric compared to conventional metrics.

### **1.4 Organization of this thesis**

This thesis is divided into 5 chapters. Chapter 2 covers retina atlas, which includes data collection, probabilistic and intensity atlas generation and application of probabilistic atlas in detection of OD and

macula. Chapter 3 introduce GMP and show its application in Optic disk and macula detection. In chapter 4 we propose Local accuracy, which is an evaluation metric to analyze vessel segmentation performance. We conclude the thesis in Chapter 5.

## *Chapter 2*

### **Optic disk and macula detection using Retina Atlas**

Accurate detection of Optic disk(OD) and macula is important as computer assisted diagnosis systems uses location of these landmarks for understanding the retina image and using clinical facts about retina for improving diagnosis. Retina landmark detection also aids in assessing the severity of diseases based on the locations of abnormalities relative to these landmarks. In this work, we first define retina atlases and then use them for OD and macula detection. Retina atlas represents the overall structure of the retina and it is inspired from the brain atlas project [34]. The data required for generating retina atlases is marked locally. We have defined 2 types of retina atlases: intensity atlas and probability atlas. We use probability atlas for OD and macula detection. The proposed system has been tested on several public datasets and obtained detection accuracy indicate comparable performance to other supervised approaches for the same problem.

#### **2.1 Introduction**

Early diagnosis and timely treatment can prevent up to 98% of severe vision loss in sight threatening diseases like Diabetic retinopathy and Glaucoma etc. Digital images of the retina acquired with or without pupil dilation, is used for screening such diseases and their automated analysis has received much attention in last two decades [30]. Accurate detection of important landmarks, namely, the OD and macula is useful in many ways: The OD location is useful to boost the bright lesion detection performance of CAD algorithms, as OD share many visual characteristics with bright lesions. The location of OD and macula aids in determining the severity of the disease and need for intervention. For instance, the proximity of a bright/dark lesion to macula indicates a higher likelihood of impaired vision and hence calls for immediate medical attention. Such precise location is also needed in registering images acquired across patient visits and assessing disease progression. In general the detection of OD and macula from colour retinal images has been treated as two separate problems, with OD detection receiving more attention than macula detection. OD detection methods typically exploit the appearance info. such as colour and roughly circular shape.

While some early attempts relied only on luminosity in the green channel, their failure in the presence of other bright lesions quickly gave rise to supervised methods. Supervised methods such as [8] [18] aims at learning the structure and luminosity distribution of OD. The performance of these methods rely on good training and test images and fixed protocol (same magnification, resolution etc.) imaging. Their performance tends to degrade on new datasets/unseen images. The roughly round shape of OD geometric modeling has also been attempted in its detection via Hough transform [20]. In addition to the high computational cost of the transform, the model fails in images with poor illumination (due to small pupil size) which renders uncertainty in the boundary between OD and background. Some other approaches to OD detection include those based on vessel crossing information [11], clustering [12], regression [16], projections along multiple directions [19] and a joint detection of macula and OD [10]. All these methods show different robustness to the presence of pathologies, uneven illumination etc. Macula detection has received relatively less attention. A common approach is to use location of detected OD for narrowing down search space [15] [9]. Regression has also been used in determining the location of macula [16]. Recently some joint detection methods [10] have been proposed, which detects both OD and macula simultaneously.

In conventional approaches, where the detected OD location is used to narrow down search space for macula, the macula detection accuracy is highly dependent on OD detection accuracy. In these approaches, it would be impossible to detect macula in case of incorrect OD detection. In this work, we present a novel joint detection approach, which simultaneously detect both OD and macula with the help of probability atlas. The probability atlas helps in utilizing spatial relationship between OD, macula and vessel arcades. We tested our algorithm on popular public datasets: messidor [35], Directdb0 [21] and drive [13]. The algorithm is giving satisfactory detection results and it is handling illumination variance and lesions well. Detailed results and comparison with other methods is also included in this chapter.

Main contribution of this chapter is experimenting with retina atlases. Intensity atlas has been explored in literature by [1] and to the best of our knowledge, we are the first one to propose probability atlas for retina images. We show the usefulness of probability atlas by proposing a system for joint detection of OD and macula using this.

Rest of the chapter is organized as follows: section 2.2 summarize the process and tool used for data marking. Section 2.3 explain the generation of intensity and probability atlas. Section 2.4 explain the system designed to detect OD and macula using probability atlas. This section also includes results, experiments and comparison with other approaches. Chapter summary is given in section 2.5.

## **2.2 Data marking**

Creation of both probability and intensity atlas requires alignment of several retina images together. For image alignment, it requires datasets along with marked ground truth. Thanks to the retina research community, there are some good quality public datasets available. Since these datasets were created and released for some specific tasks, these are marked partially. For example, largest dataset Messidor

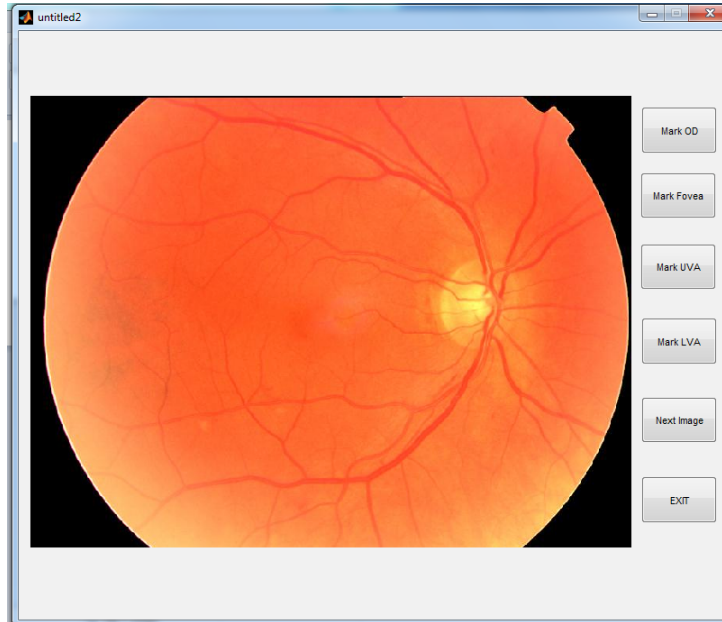


Figure 2.1: Tool for marking OD, macula and vessel arcades.

(1200 images) [35] is marked only for risk of macular edema and not for OD location, macula location and vessel segmentation. Similarly, dataset Chasedb1 [6] is only marked for vessels and not for OD and macula. Even the datasets which are marked for OD and macula generally mark OD as a point instead of an ellipse. To overcome the problem of partially marking, we marked all the popular public datasets manually for this work.

The ground truth was marked by non-field experts which was later verified by 2 field experts. In our marking process OD was marked as an ellipse, macula was marked as a point and vessel arcades were marked as curves. Vessel arcades are the primary blood vessels and out of these other small vessel branches come out. In Fig. 2.3 we have shown 1 example of upper vessel arcade(UVA) and lower vessel arcade(LVA). In our markings, only vessel arcades were marked instead of whole vessel tree. The tool for marking the ground truth was created locally in Matlab and data was saved in Matlab inbuilt .mat format. Fig. 2.1 shows a snapshot of the tool created.

One issue we faced during dataset marking is that in some images the macula is not visible. In these images, it is difficult to mark macula even by human annotator. Such images were skipped during marking and examples of few such images is shown in Fig. 2.2. Similarly, in some images there is no definitive vessel arcade present and more than 1 branch looks like vessel arcade. In these images, it is difficult to identify the correct vessel arcade. These images were also skipped during marking and an example of such image is shown in Fig. 2.2 (right most). The details of marked public datasets and actual marking statistics is given in Table 2.1. Markings for a sample image is shown in Fig. 2.3.

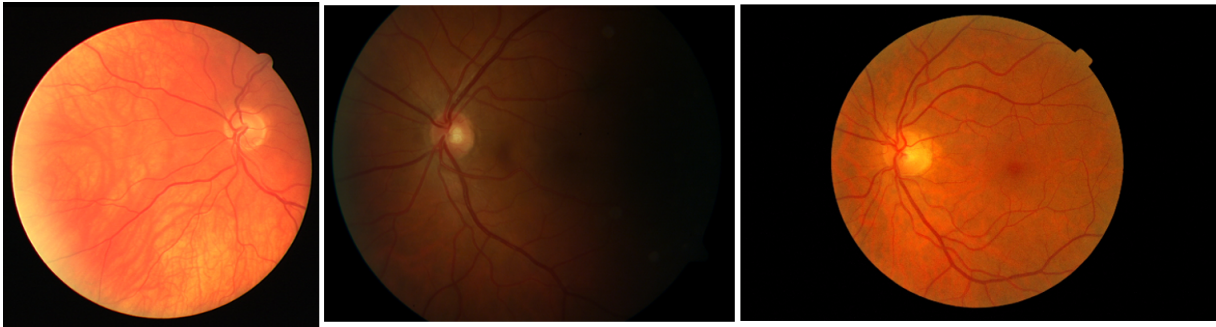


Figure 2.2: Left and center image: Skipped images because of non-visible macula. Right image: Skipped image because of non-definitive upper vessel arcade.

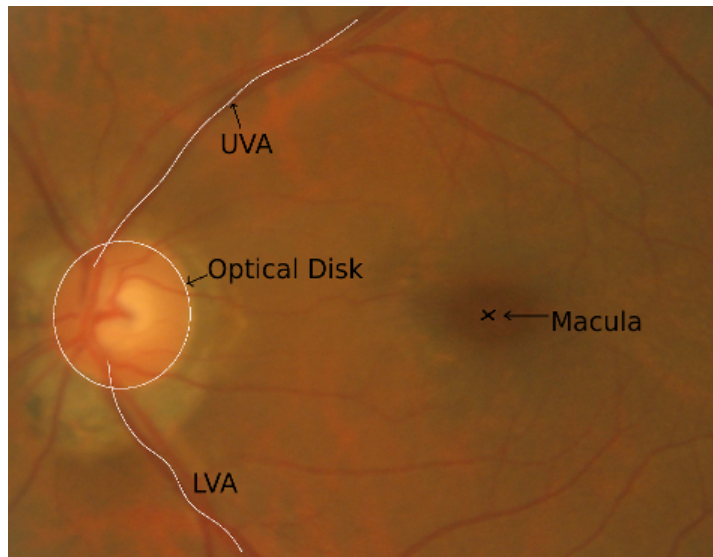


Figure 2.3: Marked data shown for a sample left eye retina image (cropped for viewing purposes)

Table 2.1: Marking statistics for public datasets.

Dataset name	Number of images	% images marked
Messidor [35]	800	87%
Drive [13]	40	92.5%
DMED [35]	160	85%
Direct-db 0 & 1 [21] [22]	800	87%

## 2.3 Retina atlas generation

Retina atlas is generated by aligning all the images together using ground truth. The generation procedure for both atlases is different and generation details of each atlas is given below

### 2.3.1 Intensity atlas generation

The intensity atlas for retina was first explored in [1] and its application was shown in exclude segmentation. The intensity atlas gives the expected intensity value for all points of retina image. Intensity atlas is similar to taking the mean of all images of dataset but since images are not aligned, some alignment is needed before taking mean and generating atlas. To generate retina atlas, we first choose a base image from dataset and we than register all the other images to chosen base image. One left and one right retina image was chosen as the base image from each dataset to obtain left and right intensity atlas. After registration of all dataset images to chosen base image, whole dataset is aligned and we combine all these aligned images to obtain intensity atlas. We use the OD, macula and vessel arcade marking information for alignment purposes and we use thin plate spline [5] as registration method.

Thin plate spline(TPS) [5] needs a corresponding set of points in both: base image and to-be-registered image for registration. We use OD location, macula location and equidistant points in vessel arcades as point set for thin plate spline registration. These points for 2 sample images is given in Fig. 2.4

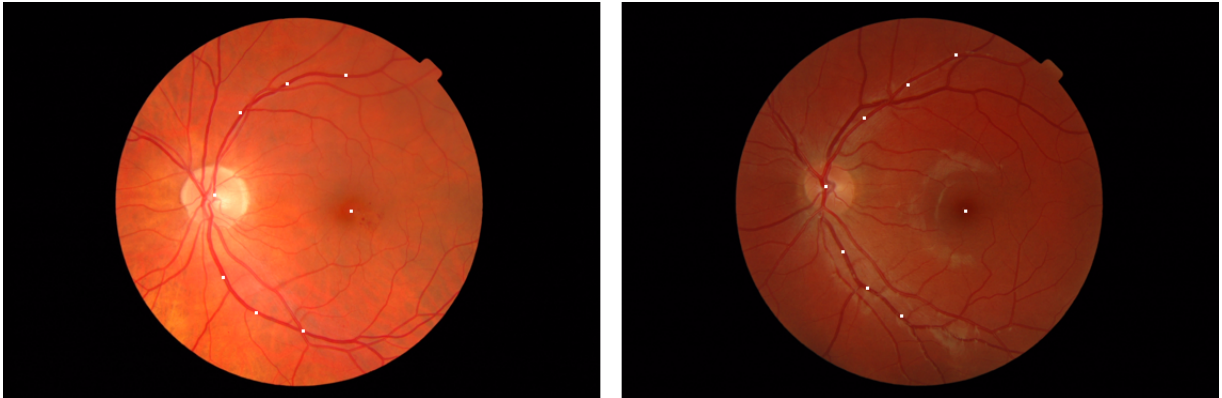


Figure 2.4: Point-sets for TPS registration. Points taken are OD, macula and equidistant points in vessel arcades.

For messidor data the chosen left and right eye base images are shown in Fig. 2.5. Finally, the left and right eye intensity atlas for messidor images are shown in Fig. 2.6.

Generated atlas completely depends on the choice of base image and since there is significant different in vessel arcade position across images, the overall atlas is irregular shaped and distorted. Since equidistant points are taken only on arcades (while doing TPS registration), vessel arcades are preserved

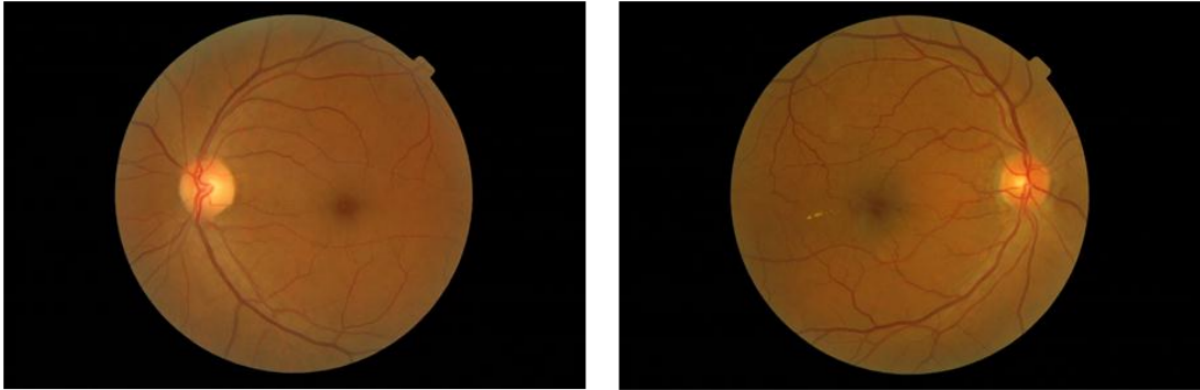


Figure 2.5: Chosen left and right eye base images for creating intensity atlas (For Messidor dataset [35]).

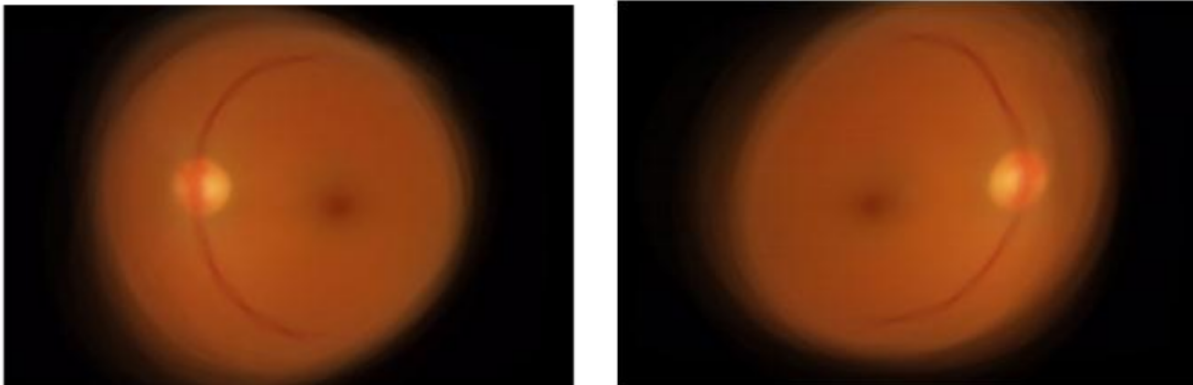


Figure 2.6: Intensity atlas for Left and right eye images (For first 400 Messidor images).

in atlas, while other vessels are completely distorted. To make the intensity atlas more stable and less dependent on chosen base image, we fit a parabola on vessel tree and take equidistant points on the parabola instead of marked image arcade. The intensity atlas after taking points on parabola is given in Fig. 2.7. We can see there is some improvement in the looks and smoothness of intensity atlas after this step.

**OD and macula detection using intensity atlas:** Our primary focus in this chapter is OD and macula detection. We tried to use intensity atlas for joint OD and macula detection. The issue we faced is that in some retina images, there is no definitive arcades present and arcade properties (like shape, angular location etc.) varies highly intra dataset. Detection of OD and macula for a new retina image will require it's registration with intensity atlas. Since registration uses vessel arcade information, we will need to accurately segment vessel arcade before attempting OD and macula detection. Since accurate vessel arcade detection is even tougher problem and some images don't even have definitive

arcades (example Fig.2.2), we can't be dependent on it for registration. For parabola based intensity atlas, the same problem lies in the good estimation of parabola. Since our intensity atlas fails to provide good results, we proposed and explored probability atlas for joint OD and macula detection. To the best of our knowledge, the probability atlas has not been explored in literature. The details of probability atlas and its application in joint OD and macula detection is given in next section.

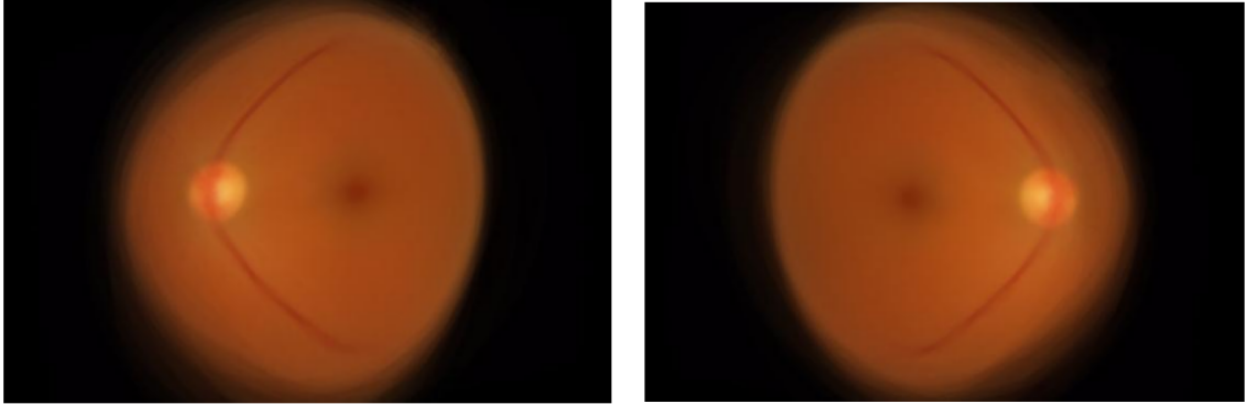


Figure 2.7: Left and right eye intensity atlas for first 400 Messidor images. Here arcades are represented by parabola and equidistant points are taken on parabola.

### 2.3.2 Probability atlas generation

The probability atlas gives relative positioning of different landmarks in retina images. The value at each point in probability atlas gives it's probability of being certain landmark. The idea here is to represent relative positioning of OD, macula and vessels for the whole dataset in an atlas image and use this atlas image for detection of OD and macula. Alignment of all images for the given dataset is required to generate probability atlas.

We use similarity transform for aligning all images together. Similarity transform needs two matching points for getting transformation function and we use marked OD and macula location for this. All left eye images are aligned and combined to get left eye probability atlas and all right eye images are aligned and combined to get right eye probability atlas. Unlike intensity atlas, we don't choose base image in probability atlas creation but we fix the location of OD and macula in target atlas image. For an image dataset of  $R$  rows and  $C$  columns, the transformation points in target atlas image are fixed at  $(0.5 \times R, 0.25 \times C)$  for OD and  $(0.5 \times R, 0.25 \times C + Dist)$  for macula. Here first and second value inside bracket represents the row and column position respectively.  $Dist$  is the distance between OD and macula in reference image. So basically during atlas creation, we are transforming every image in input dataset such that after transformation all Optic disks gets mapped to same location in atlas. Similarly all macula points get mapped in the same row as OD, while maintaining original distance between

OD and macula. After getting transformation function, we calculate OD, macula and vessel probability atlas. The methods for generating OD, macula and vessel arcade probability atlases is explained below:

- **OD probability atlas generation:** During ground truth marking, OD was marked as an ellipse. A binary mask for OD is obtained such that the intensity value of this binary mask is 1 for all points inside ellipse and 0 outside it. The center of this ellipse is used as the OD location for reference image in similarity transformation. After transformation, this binary mask is averaged over all images to get OD probability atlas.
- **Macula probability atlas generation:** During ground truth marking, macula was marked as a point. Since the macula is marked as a point, after alignment the macula position will be represented by some discrete points on horizontal line. Each one of these points corresponds to an image of input dataset. To make the atlas smooth, a normalized Gaussian function of  $0.5 \times R$  variance is placed on these discrete macula points. Here  $R$  represents average OD radius for our dataset. The normalized sum of these Gaussians is taken as macula probability atlas.
- **Vessel arcades probability atlas generation:** Vessel arcades are primary vessel in vessel tree and during marking they were marked as a curve. To generate vessel arcade probability atlas, we represent vessel arcades by a set of points. The samples points are taken equidistant (angle wise). The angle range for left eye image is 45-120 degree for upper vessel arcade and 225-290 degree lower vessel arcade. A Gaussian function of  $0.5 \times R$  variance is placed on these sample points and normalized sum of all these Gaussians is taken as arcade probability atlas. This sampling process is also shown in Fig. 2.8

Now we have 3 probability atlases corresponding to OD, macula and vessel arcades, we represent all these maps in one image by using 3-channel color image and call this color image our probability retina atlas. We show OD, macula and arcade probability atlases by red, blue and green channel respectively. Probability atlas for first 400 messidor [35] images for both eyes is shown in Fig. 2.9. The shown probability atlas is cropped and normalized for visualization purposes.

## 2.4 OD and macula detection using probability atlas

For a new retina image, we detect it's OD and macula by registering it to probability atlas. In order to register any new image to atlas, we first make initial estimations for OD, macula and vessel arcades. The aim here is to get candidate points for OD, macula and vessel arcades rather than exact detection. OD and macula is than jointly detected by registering the candidate points to probability atlas. The method for candidate points detection for each landmark and joint detection is given in sections below.

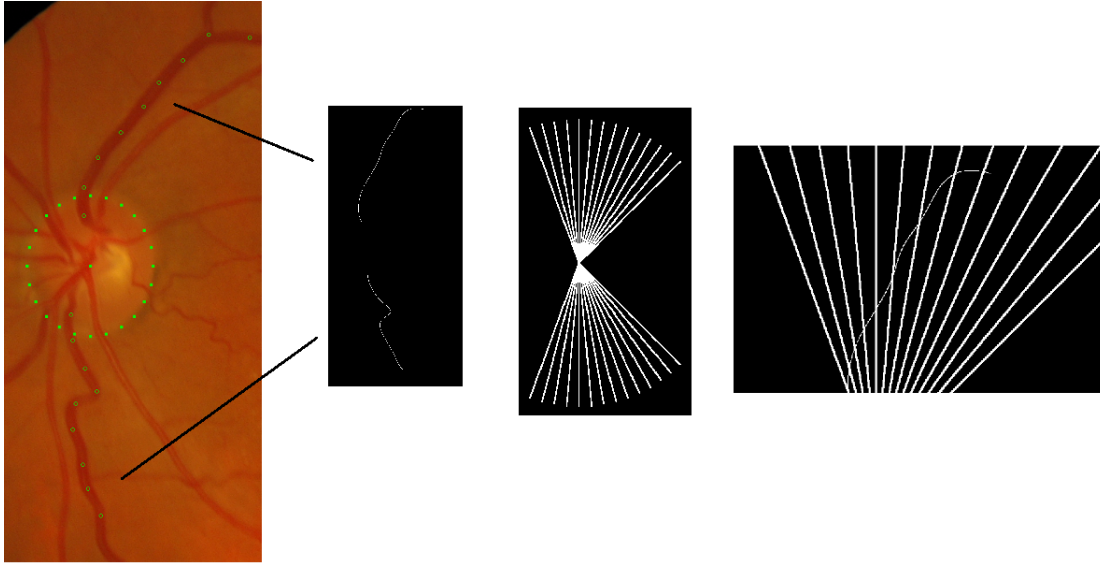


Figure 2.8: Vessel arcade sampling for vessel probability atlas generation.

### 2.4.1 OD detection

OD is a bright, elliptical structure from which blood vessels come out. After examining few retina images visually one can make following observations about OD structure.

1. The OD region is locally bright and the average brightness difference between its immediate and distant neighborhood is high.
2. Vessel density around this region is high since all blood vessels emerges from this region including vessel arcades. This property helps in discriminating OD from other bright regions in image.
3. Its shape is circular or near circular (elliptical).
4. The vessels around it are in vertical direction.

We find OD candidates using above properties and we only use green channel of raw image for this. Raw intensity values of smoothen image, intensity difference between immediate & distant neighbors and vesselness sum in immediate neighborhood are used as features. Here immediate neighbors are pixels within  $R$  distance and distant neighbors as pixels between  $R - 1.5 \times R$ . Here  $R$  is average OD radius for current dataset, which we can get from our probability atlas. All these features are first normalized and then combined (with equal weight) to get OD feature map. This OD feature map for a sample image is shown in Fig. 2.10. We find local maxima of this OD feature map to get OD candidates. We know that near OD, the direction of vessels is vertical. The sum of horizontal gradients on the vessel tree around candidate points is found and thresholded to reject some candidate points.

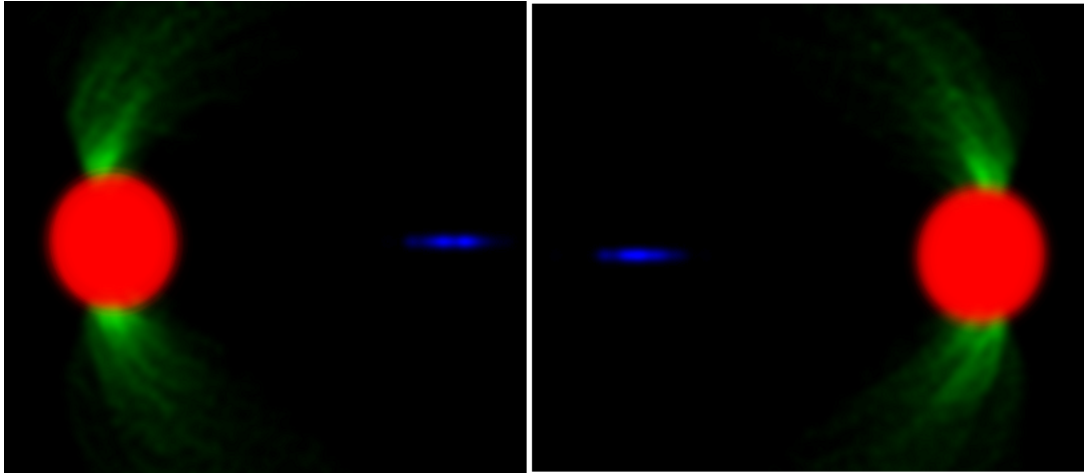


Figure 2.9: Probability retina atlas for left and right eye. Red, blue and green channel represents OD, macula and arcade probability atlases respectively.

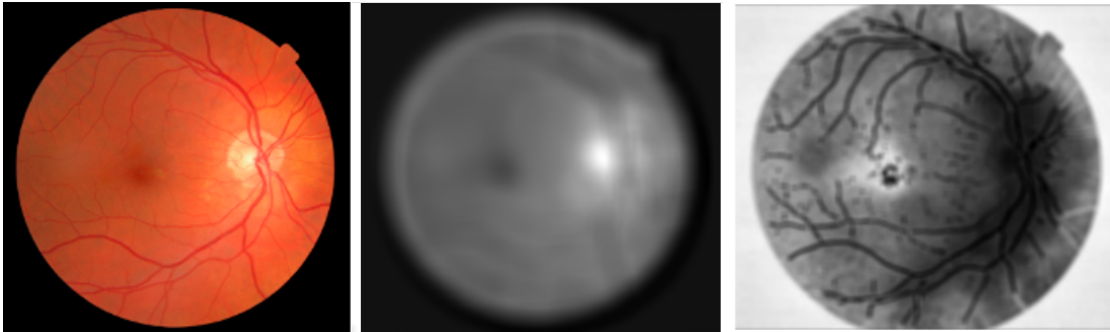


Figure 2.10: Left to right: Sample retina image, OD feature map, macula feature map.

### 2.4.2 Macula detection

Macula is locally dark and small irregular shaped region where vessels are not present. This area forms the center of retina and it is responsible for high vision as this is the area where the density of cones are highest. Following observations can be made about macula region:

1. The region is locally dark and its structure and boundary are not well defined.
2. The vessel density around macula is low, this condition helps in distinguishing macula from other dark lesions and vessel structure.
3. Its location is highly related with OD location because it is a clinical fact that the distance between OD and macula is 2.5 times diameter of OD.

4. If we define a hyper line which cuts vessel tree in halves and pass through OD, the macula will either lie on this line or the distance will be very low.

We use smoothen raw intensity values and vesselness sum in immediate neighborhood as features for generating macula feature map. Both features are first normalized and then combined (with equal weight) to get macula feature map. This macula feature map is calculated for each test image and it is different from macula probability atlas, which is generated for a dataset. This feature map for a given retina is shown in Fig. 2.10. Notice how the regions with actual location of macula are darker compared to rest of the image, since both intensity values and vessel density are lower at this region. We take local minima of macula feature map as candidates for macula center.

### 2.4.3 Vessel arcade detection

Vessel arcades are the master branch of vessel tree and they are detected by taking top vessels from vesselness map. For calculating vesselness map, we use [25], which first calculates  $2 \times 2$  Hessian matrix for each pixel and then uses eigenvalues of this Hessian matrix for the calculation of vesselness measure. For vessel arcades, this vesselness value is higher than rest of the vessel tree, so taking top pixels from this vesselness image gives us a poor estimate for vessel arcades. We choose [25] method because it is fully unsupervised and fast enough for our purpose. The vesselness image and detected vessel arcades for a sample image is shown in Fig. 2.11.

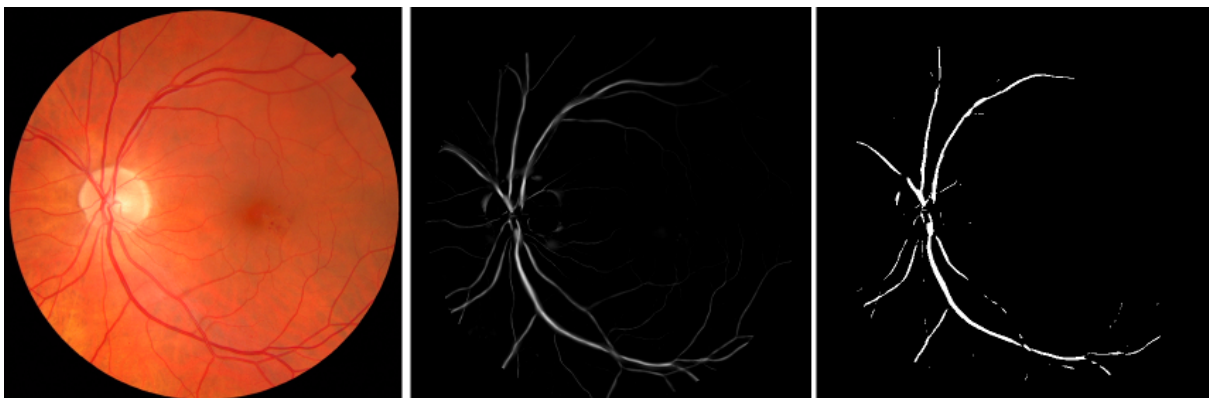


Figure 2.11: From left to right: Sample image, vesselness image using [25], Detected vessel arcades.

### 2.4.4 Joint OD macula registration

After getting candidate points for OD, macula and initial estimate of vessel arcade for input image, we find the OD, macula pair which agrees the most with our probability atlas. We find atlas agreement score for each pair and the pair with highest atlas agreement is declared as final detected pair.

If there are  $M$  and  $N$  candidate points for OD and macula respectively, we examine  $M \times N$  OD, macula pairs and we choose the winning pair among them. For an OD candidate  $m$  and macula candidate  $n$ , we transform the OD feature map, macula feature map and estimated arcades using similarity transform. The transform function is obtained by mapping  $m$  to OD and  $n$  to macula center of probability atlas. After transformation, the “matching score” for OD is calculated by comparing OD feature map around  $m$  with OD probability atlas. Similar “matching score” of macula is calculated by comparing macula feature around  $n$  with macula probability atlas. Upper vessel arcade and lower vessel arcade matching score is also calculated in similar manner.

The comparison function, we use the sum of point wise multiplication of rectangle around given candidate point  $m$  and  $n$ . The size of the taken rectangle for comparison is  $(R \times R)$ ,  $(2R \times R)$  and  $(0.5R \times R)$  for OD, vessel arcade and macula respectively. Here first value of bracket is number of rows and second value is number of columns.  $R$  here represents the OD radius, which we get from atlas. Overview of our system is given in Fig. 2.12.

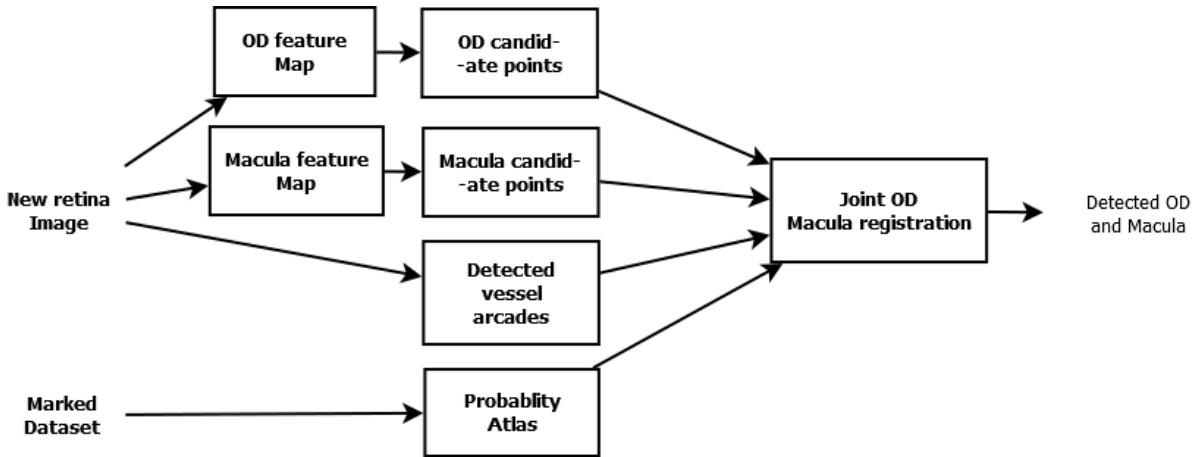


Figure 2.12: Overview of our work.

### 2.4.5 Experimental results

We have evaluated our algorithm on popular public datasets, such as messidor [35], drive [13] and direct-db0 [21]. The results for these datasets and comparison with recent work [17] are included in this section.

Fig 2.13 shows qualitative results of our joint OD macula detection for a few retina images. Our algorithm can handle small illumination variance and lesions presence but it fails in the case of uneven illumination.

The detection rates for OD and macula detection for 3 public datasets are shown in Table 3.2 and Table 3.3 respectively. Both OD and macula detection rates are on the marked subset of dataset instead

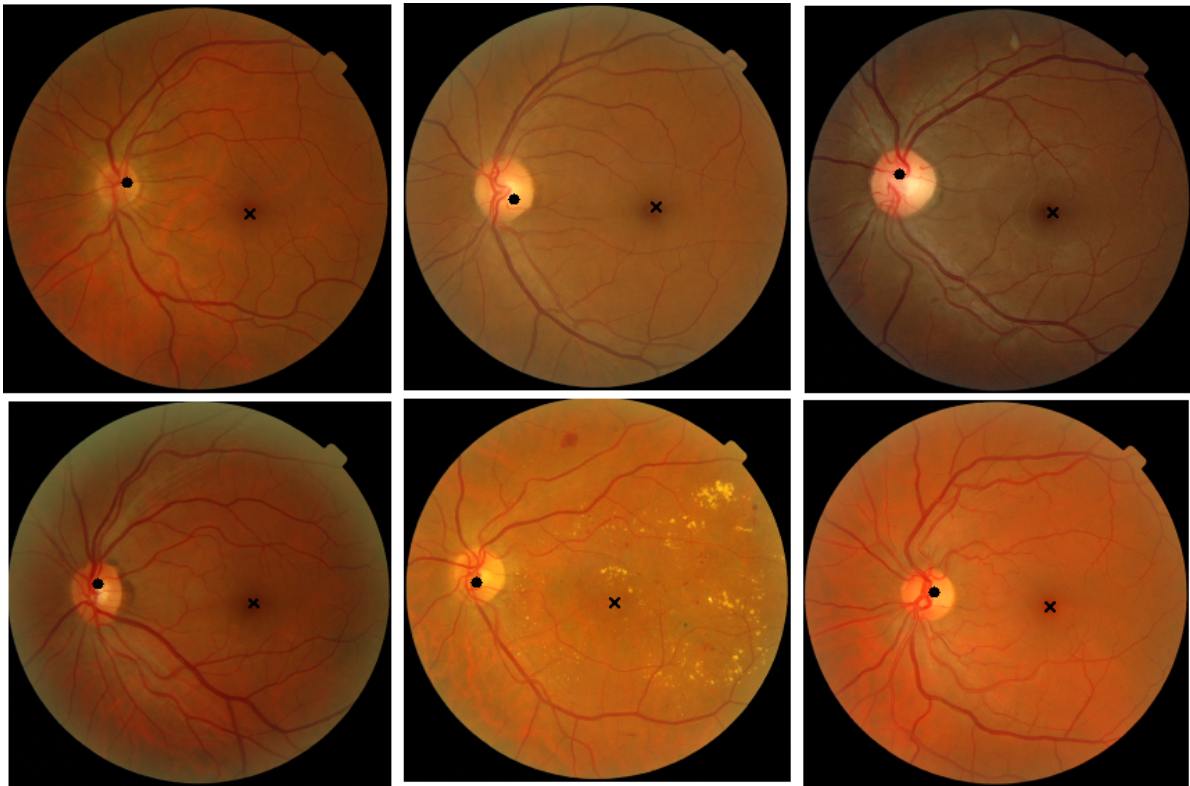


Figure 2.13: Output of the algorithm on sample images from messidor [35]. OD is marked as black dot and macula is marked as black cross.

Table 2.2: Comparison of OD detection rates on popular datasets

Detection rates %	Our	[17]
Messidor (first 800 images with pupil dilation)	93.4	-
Drive (20 images)	100	100
Directdb0 (131 images)	97.11	97.64

Table 2.3: Comparison of detection rates for macula on popular datasets

Detection rates %	Our	[17]
Messidor (first 800 images with pupil dilation)	90.7	-
Drive (20 images)	90	91.73
Directdb0 (131 images)	96.34	96.79

of whole data, because we skipped some images during marking as explained in section 2.2. In this work, probability atlas that is used for detection is from first 400 messidor images and same atlas is used for Drive and Direct-db after scaling according to image size of test dataset, which makes our atlas robust across datasets. The metric used in evaluation is same as [17]. The detection is considered successful, if it falls within a certain range of ground truth. As we can see from the results, the detection rate of our algorithm is slightly lower than [17].

## 2.5 Summary

In this work, we explored retina atlas with the focus of finding their application in OD and macula detection. We marked a lot of data manually for this work and defined intensity and probability atlases. We tried to use these intensity atlases and did use probability atlas for OD and macula detection.

The OD and macula detection accuracy with probability atlas indicates that the algorithm works reasonably well on public datasets. The algorithm is supervised but it also needs vessel arcade information along with OD and macula location for training, which is a downside of our algorithm. The results are satisfactory but simpler approaches outperform our detection accuracies, so it's not very practical. Although the algorithm itself is fast and our unoptimized Matlab code takes about 10 seconds for each image on a single threaded environment. The reason our accuracy is not great is because we are not able to get good macula feature map and arcade estimation. In the end, results were not satisfactory but this chapter serves as an important experiment as we tried something new with retina images and discussed the outcome. To get better detection accuracy, we have proposed fully unsupervised GMP based approach for OD and macula detection in next chapter.

## Chapter 3

### Optic disk and macula detection using Generalized Motion pattern

Accurate detection of optic disk and macula are of interest in automated analysis of retinal images as they are landmarks in retina and their detection aids in assessing the severity of diseases based on the locations of abnormalities relative to these landmarks. The general strategy in the literature is to design different methods for each of these landmarks. In contrast, we propose a novel and unified approach for Optic disk and macula detection in this paper using the Generalized Motion Pattern (GMP) [14] [23]. GMP is derived by inducing motion to an image to smooth out unwanted information, while preserving the structure of interest. The proposed method is unsupervised, parallelizable and handles illumination differences efficiently but assumes a fixed protocol in image acquisition, which is generally true and its true for all public datasets related to retina. The proposed method has been tested on five public datasets and obtained results indicate superior performance compared to other unsupervised approaches and comparable performance to supervised approaches for the same problem.

#### 3.1 Introduction

The aim and motivation of detecting optic disk and macula is same as previous chapter, as we are attempting to solve the same problem using different approach. Last chapter also includes literature survey and problem background so we will skip that part here.

We aim to detect OD and macula using a unified approach which uses the concept of Generalized Motion Pattern (GMP) that was introduced in [14]. In [14] the authors demonstrated its usefulness for global detection of abnormalities from mammograms and retinal images. The GMP is derived by inducing motion to an image, which serves to smooth out unwanted information while highlighting the structures of interest. This concept was extended in [23] by inducing a set of motions to a given image. The results of these induced motions are then combined to construct an *Interference map*. This interference map was demonstrated to be useful in building an assistive tool for local lesion annotations. In this work, we demonstrate how this concept of interference map can be applied to the problem at hand: OD and macula detection.

The main contribution of this work is an unsupervised, parallelizable OD and macula detection algorithm for fixed protocol DR datasets. The method is highly robust to uneven illumination and small pathologies. Our method does not require much parameter tuning and we have used same set of parameters for all the 5 public datasets we reported the results on, which is another big contribution.

Rest of the chapter is organized as follows: Section 3.2 summarize the concept of GMP and interference map. Section 3.3 presents the proposed approach for OD and section 3.4 presents the proposed approach for macula detection. Section 3.5 explains the experiments done and it also reports results on 5 public data-sets. Comparison with recent work is also included in this section. Conclusion and scope for future work is given in section 3.6.

## 3.2 GMP and interference map

For a given gray scale image  $I$ , its GMP representation  $I_{GMP}$  [14] is defined as

$$I_{GMP}(\vec{r}) = f(I(T_j(\vec{r})|1 \leq j \leq N)) \quad (3.1)$$

Here  $\vec{r}$  denotes the pixel location,  $T_j(1 \leq j \leq N)$  denotes  $j^{th}$  rigid transformation applied to  $I$  which produces  $j^{th}$  resultant image. Total of  $N$  rigid transformations are applied and  $N$  resultant images are produced. These images are combined into the GMP map using a coalescing function  $f(\cdot)$ .  $f(\cdot)$  maps the set of pixel intensities at each location ( $\vec{r}$ ) across the transformed images to a scaler value in produced GMP image.

**GMP interference map generation:** The combination of a family of GMPs generated by inducing rotation motion in a given image is defined as an interference map [23]. For a given image  $I$ , let the GMP with rotation about a pivot  $P_k$  be  $I_{GMP}^k$ . An ensemble of  $K$  GMPs is generated when  $K$  pivot points are chosen:  $C_K = \{I_{GMP}^k|1 \leq k \leq K\}$ . The interference map  $I_{int}$  is generated from  $C_K$  as follows

$$I_{int}(\vec{r}) = \phi(C_k) = \phi(\{I_{GMP}^k(\vec{r})|1 \leq k \leq K\}) \quad (3.2)$$

where  $\phi(\cdot)$  maps the ensemble of GMPs to a single interference map.

Each  $I_{GMP}^k$  is generated using eq. 3.1, with  $T$  as rotation by an angle in the range  $(-\theta, \theta)$  degrees in steps of 1 degree. The coalescing function  $f(\cdot)$  can be chosen as min, max and median, which generates minimum GMP, maximum GMP and median GMP respectively. The rotation range  $(-\theta, \theta)$  controls the degree of rotational motion.  $\phi(\cdot)$  was chosen to be a mean function in the past works [23]. In this work we choose  $\phi(\cdot)$  as pointwise quartile generator which generates quartile intensity value for  $I_{int}(\vec{r})$  from GMPs with  $K = 150$  randomly chosen pivot points. Fig. 3.1 shows a sample image and corresponding min and max GMP interference maps. For these min and max interference GMP, the  $\phi(\cdot)$  was chosen as mean function. As you can see in max interference map, bright structures are highlighted and everything else is suppressed. Similarly in min interference map dark structure (macula) is highlighted and everything else is suppressed. These interference maps are normalized for viewing

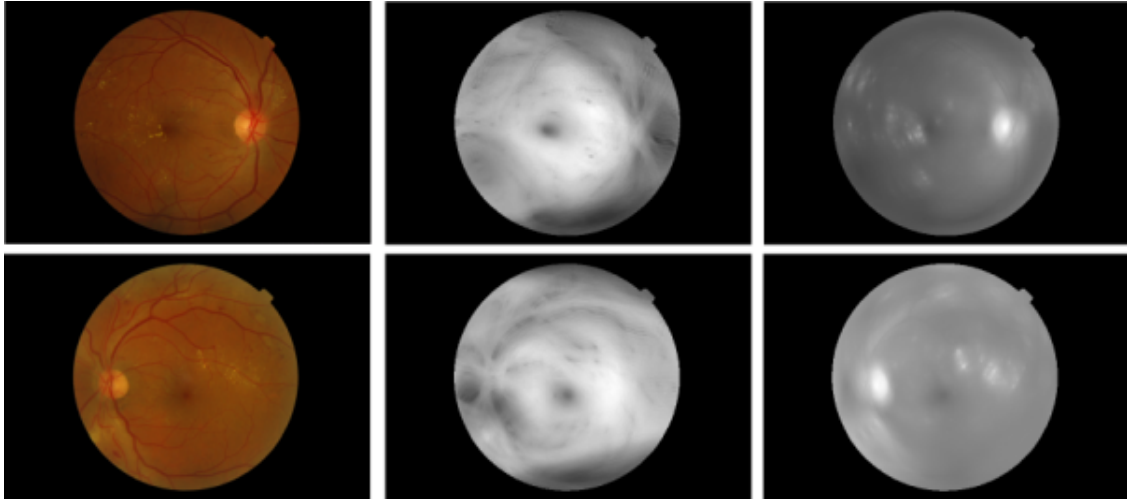


Figure 3.1: From left to right: Original image, min GMP and max GMP interference map. In these maps, coalescing function  $f(\cdot)$  is max/min and  $\phi(\cdot)$  is mean. These interference maps are normalized for viewing purposes.

purposes. For the detection of OD, we want to highlight OD region. The problem with max interference is that it highlights all bright structure, so if there are bright lesions in image they get highlighted too. In this work, we propose median GMP interference map which only highlights Optic disk and suppress local brightness and bright lesions. Fig. 3.2 shows two sample images and their corresponding GMP and the final median interference map. The shown GMP is corresponding to the pivot point marked as cross. Both the GMP and final median interference map are normalized for viewing purposes. The blur seen in the GMP is due to the induced rotational motion. Since we choose pivot points at random, this blur cancels out in final combined interference map. The interference map is seen to effectively localize OD as a bright region, while suppressing minor vessels and the bright circular artifacts (due to laser surgery). This is notwithstanding the poor illumination in the image (bottom row). Fig. 3.3 compares median GMP interference with max GMP interference in case of high number of lesions. This demonstrate the usefulness of median GMP in case OD detection. The bright lesions have been effectively suppressed in median GMP interface image.

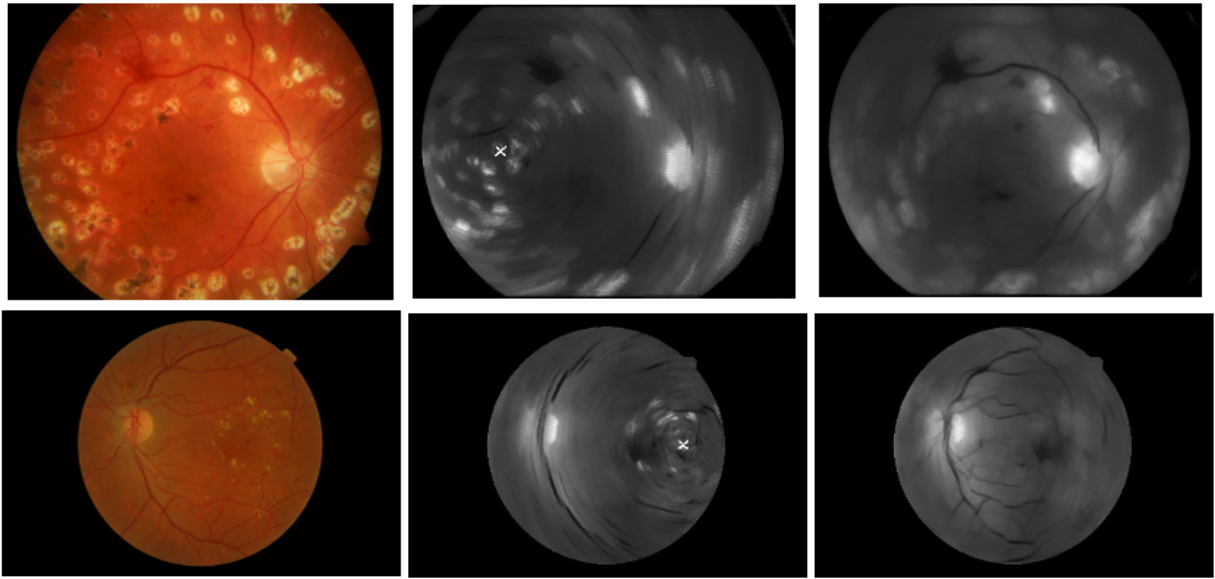


Figure 3.2: GMP and interference map for samples images from Directdb (top row) and Messidor (bottom row). From left to right: original image, GMP about the pivot shown as white cross and interference map.

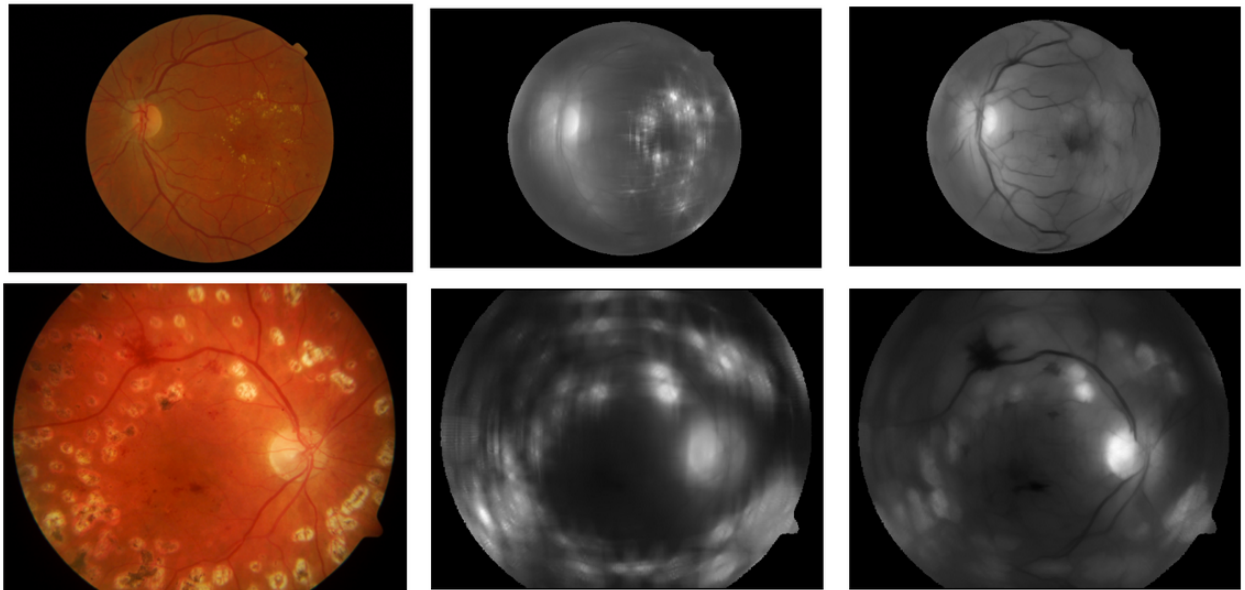


Figure 3.3: max and median interference map for samples images from Messidor (top row) and Directdb (bottom row). From left to right: Original image, max interference map with  $f(\cdot)$  as max and  $\phi(\cdot)$  as mean and median interference map with  $f(\cdot)$  as median and  $\phi(\cdot)$  as quartile point generator.

### 3.3 Optic disk detection using interference map

Our OD detection pipeline consists of two major stages. Stage one is candidate selection which is based on interference map and stage two is candidate rejection which is based on domain knowledge-based cues.

#### 3.3.1 Optic disk candidate selection

The optic disk candidate selection is based on an observation from the  $I_{int}$ , that the intensity value in the OD region is higher than background and the intensity value decreases as we move away from OD center.

Optic disk candidates are obtained from a series of  $j$  binary maps where  $I_{bin}^j$  obtained as follows.

$$I_{bin}^j(\vec{r}) = \begin{cases} 1 & \text{if } I_{int}(\vec{r}) > I_{high} - j * step\_size \\ 0 & \text{otherwise} \end{cases} \quad (3.3)$$

$$step\_size = (I_{high} - I_{low})/20 \quad (3.4)$$

Here  $\vec{r}$  represents each pixel location,  $I_{high}/I_{low}$  are the highest/lowest intensity value of  $I_{int}$  and  $j$  is from 1 to 6.

Note that  $I_{bin}^1$  binary image will have lowest number of candidate regions, while  $I_{bin}^6$  will have maximum. The geometric center of the candidate region in  $I_{bin}^j$  with the lowest  $j$  index is taken as the candidate OD center. These binary maps for a given GMP interference image are shown in Fig. 3.4. Detected candidate points are also marked in these binary maps. It is worthwhile to note that in 75-80% of retinal images, there is only one candidate point passed by this stage. However, to handle the cases with multiple candidates (due to pathologies or artifacts) a rejection scheme is required which is described next.

#### 3.3.2 Determining the final optic disk location

Three, rule-based, unsupervised, rejection stages are designed to determine the final OD center by choosing the best possible candidate points from detected candidate points. The first 2 rejection stages are based on vessel information and the 3<sup>rd</sup> rejection stage uses previously detected OD position information and assumes a fixed protocol across images, which is generally true in image acquisition for a specific dataset.

1. **Rejection based on vessel direction:** This rejection stage is based on the observation that near OD, the direction of vessels is vertical. This rejection stage gives good horizontal localization by rejecting candidates caused by bright lesions. The sum of horizontal gradients on the vessel tree around candidate points is found in a  $m \times n$  rectangular box with  $m = 2n$ . This sum is thresholded

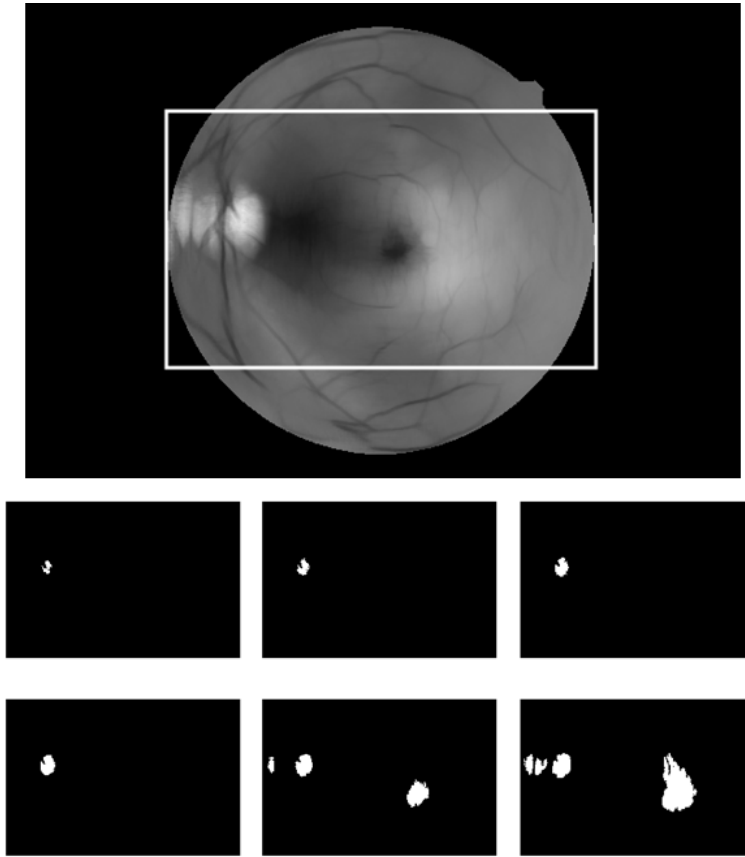


Figure 3.4: Example GMP interface map and respective binary maps. Binary maps are shown only for rectangular area marked by white lines in interference image.

to perform the rejection. The horizontal gradients are extracted from segmented vessel tree using an unsupervised vessel segmentation method [25].

2. **Rejection based on vesselness sum:** OD is a bright region where vessels exit the retina. Hence, candidates that do not enclose vessels can be rejected. This is done by computing the vesselness or the probability of a pixel being the part of a vessel. The sum of vesselness values in a square region around a candidate is found and thresholded to reject false candidates which typically occur in the bright regions above and below the OD. The method used for the calculation of vesselness is [25]. For a sample image the vesselness and horizontal gradient is shown in Fig. 3.5.
3. **Rejection based on expected Optic disk location:** This stage assumes that a fixed protocol has been used for image acquisition, which is generally true. Fixed protocol limits the possible locations where OD is highly likely to be found in a given image. This can be found offline, using the ground truth. We used an alternate method using a 2-pass strategy where all the images with

single detected candidate for OD were used to find the set of possible OD locations  $S : \{r_n^{\vec{}}\}$ . By clustering  $r_n^{\vec{}}$  values,  $S$  is partitioned into 2 subsets, one each, for the left and right eye. These subsets aid defining the mean OD locations for the right and left eyes:  $r_R^{\vec{}}$  and  $r_L^{\vec{}}$ , for a given dataset. In the 2nd pass, images with multiple candidates were processed using the distance of candidates to  $r_R^{\vec{}}$  and  $r_L^{\vec{}}$ , to retain the candidate with minimum distance as the final OD center  $r_{OD}^{\vec{}}$

Fig. 3.6 shows a sample image and its computed  $I_{int}$  where 5 candidates were found. The OD region is not well delineated in  $I_{int}$  as there is also a bright region below it. Nevertheless, the 3 rejection stages successfully eliminate the false candidates (1 each by the first two stages and 2 by the third stage) and retain the correct candidate (in green box).

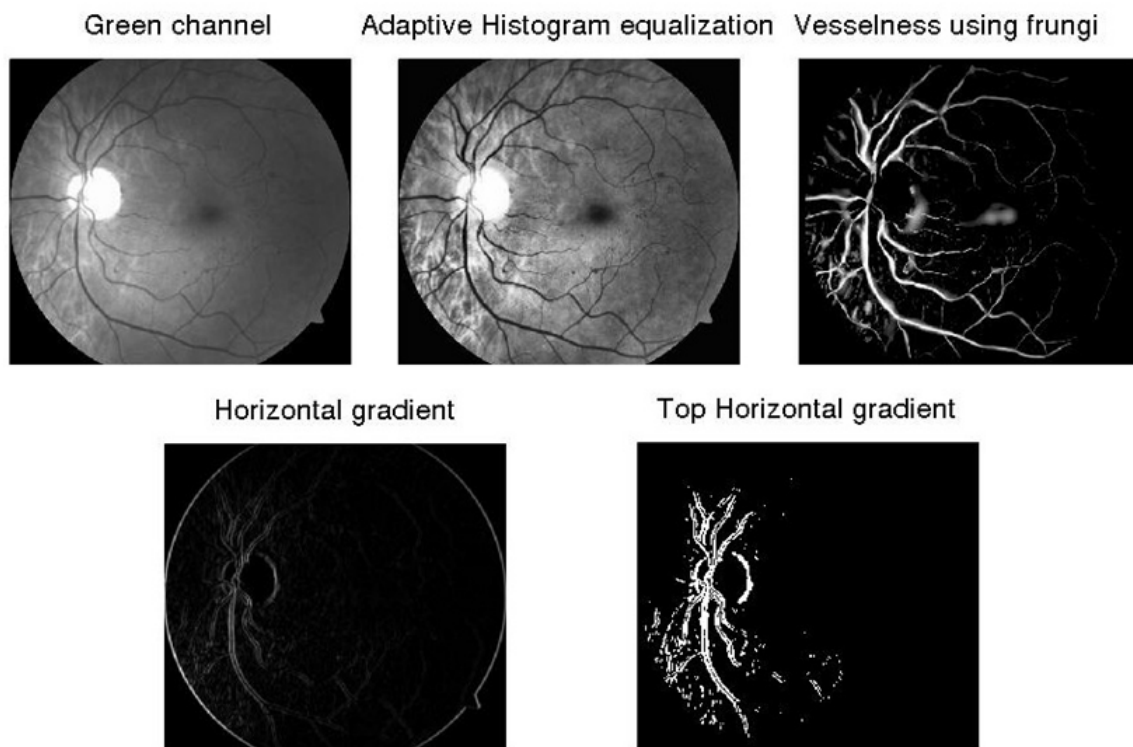


Figure 3.5: Example image and respective vesselness and horizontal gradient image.

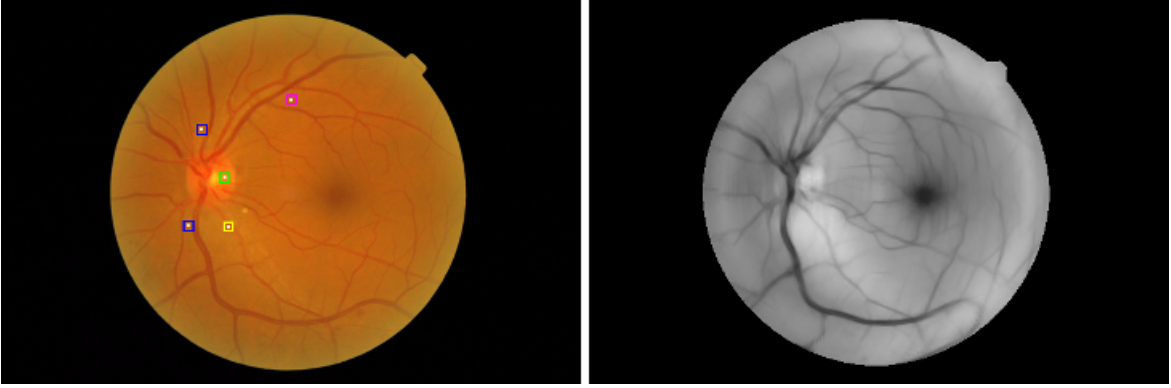


Figure 3.6: Example image and respective interference map with candidate points shown as white dots. Pink, yellow and blue squares represents rejection because of stage 1,2,3 respectively. Final detected OD is surrounded by green square.

### 3.4 Macula detection using detected optic disk

It is a clinical fact that the distance of macula center from optic disk center is roughly 2.5 times diameter of the OD. The macula appears as a dark region bereft of vessels. In this work, we use the computed position of OD to narrow down the search space for macula detection. Determining the accurate OD radius for each image is a very challenging task so instead of defining the macula search space in terms of OD radius, we define it as a ratio of image FOV (the circular bound of the image) radius with respect to detected OD location  $r_{\vec{O}D}$ . Since the relation between OD radius and image FOV radius depends on image magnification, this search space is slightly different for each dataset. However, in our experiments, it was observed this variation is negligible and general parameters can be used.

Since macula is the darkest region locally, the green plane of macula search space of the given image ( $I_{sub}$ ) is processed to generate several binary images using multiple thresholding. The idea here is similar to the one we followed for OD candidate generation.

$$I_{bin}^k(\vec{r}) = \begin{cases} 1 & \text{if } I_{sub}(\vec{r}) < I_{low} + k \times step\_size \\ 0 & \text{otherwise} \end{cases} \quad (3.5)$$

Here  $I_{sub}$  is cropped sub-image and  $I_{low}$  is lowest intensity in sub-image. In our implementation,  $k = 1 : 10$  and  $step\_size = (I_{high} - I_{low})/20$ , which means that we are assuming that fovea lies in the bottom 50% intensity range and its center is darker than its surroundings. These parameters ensure adaptation to an image and hence robustness across datasets.

After generating multiple binary images macula center candidates are generated in a similar manner as OD candidates. In rare cases where there are multiple candidates, the candidate closest to sub-image  $I_{sub}$  center is chosen as the macula center. The overview of our system is given in Fig. 3.7.

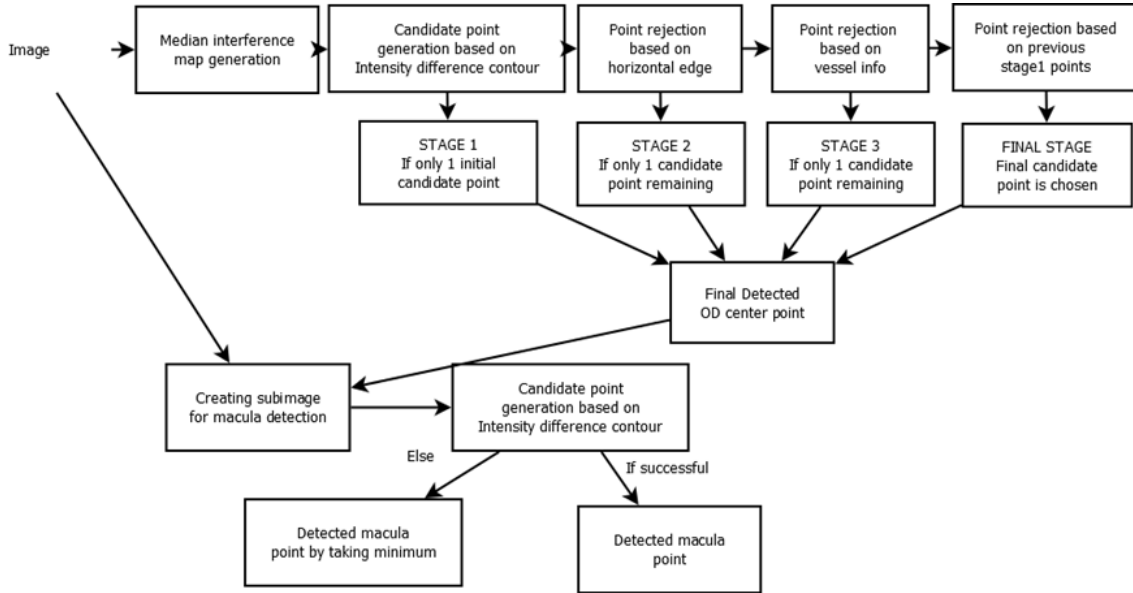


Figure 3.7: Overview of over system.

### 3.5 Results and Experiments

The proposed method was evaluated on 5 public datasets including Messidor [35], Diaret-db0 [21], Diaret-db1 [22], DMED [37] and DRIVE [13]. Only DRIVE had OD and macula markings available publicly. Annotations for other datasets were obtained locally, while marking the data for Atlas creation. OD was marked as an elliptical disk and macula center was marked as a point. OD was marked on all the images and since the macula location is not clear in some images, those images were skipped during macula marking.

Messidor dataset has 1200 high resolution images out of which first 800 images are acquired after pupil dilation. First 800 images from Messidor, all 130 images from Diaretdb0, all 89 images from Diaretdb1 and all 169 images from DMED were marked for OD and macula. All of these datasets has significant variance in terms of abnormality distribution, brightness, illumination etc. Within each dataset FOV and magnification is similar and all of these datasets are macula centered.

Table 3.1 reports the results for OD detection and OD localization accuracy. OD is considered to be correctly detected if the detected OD lies within the marked elliptical OD boundary. We also report localization accuracy in terms of distance from center of OD, normalized by mean OD radius  $R$  which is calculated for each dataset using marked elliptical boundary. Our method has good localization accuracy because OD center is characterized by high intensity values in  $I_{int}$ .

Table 3.2 compare our method with other recent works. As we can observe, our method consistently outperforms the unsupervised algorithm [2] and is comparable in perform with ensemble based super-

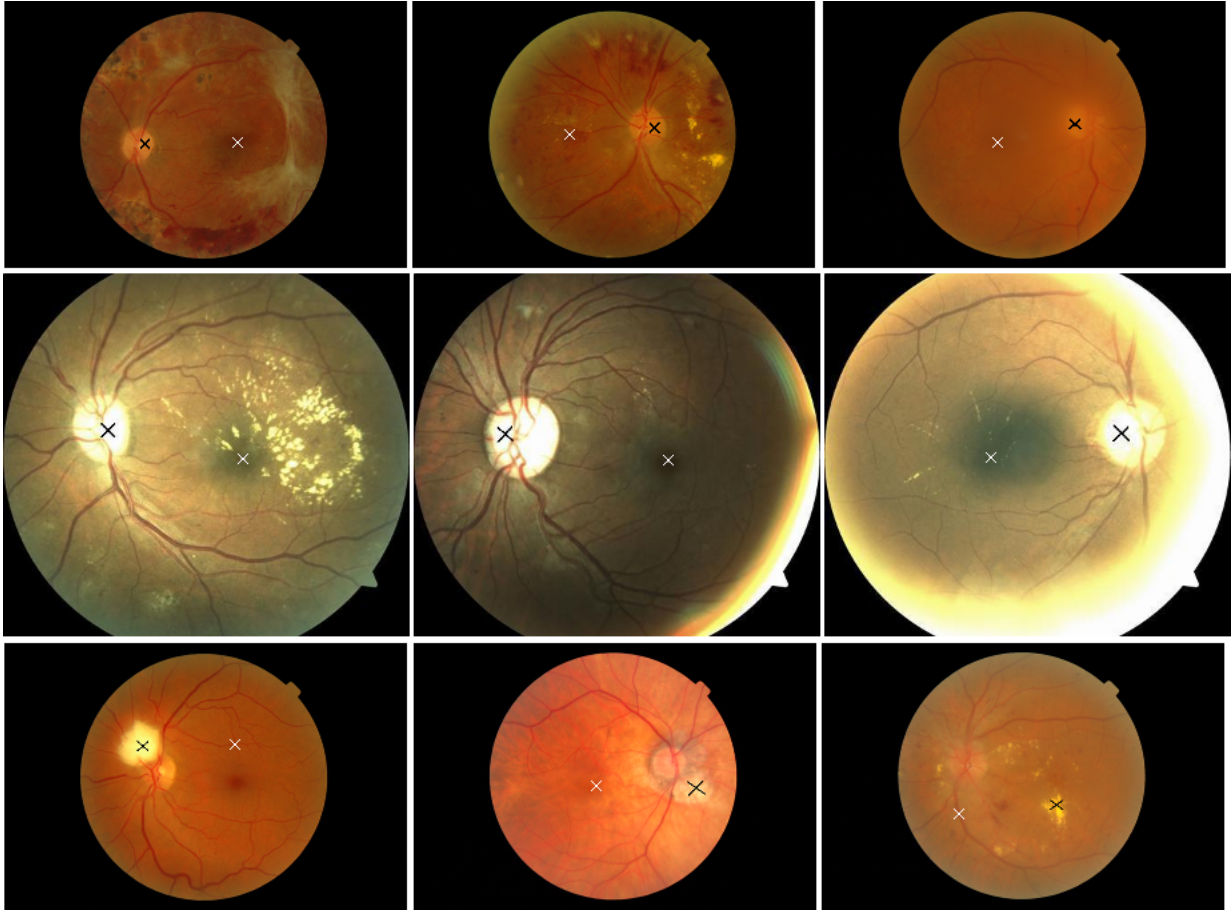


Figure 3.8: OD and macula detection results (Black cross represents OD and white cross represents macula). Top two rows show correct detections in images from Messidor and DMED, respectively. Last row shows failure cases (from left to right) due to image capture, failure in rejection stages and presence of large pathologies.

Results	Optic disk				
	Accuracy	% images within ( $R$ is avg. OD radius)			
		$R/4$	$R/2$	$R$	$2R$
Messidor(first 400)	98.50	84.25	98.5	99	99.5
Messidor(400 - 800)	98.25	85.25	98	99	99.75
Directdb0(130 images)	96.15	82.31	96.92	97.69	98.46
Directdb1(89 images)	95.51	82.02	94.38	97.75	97.75
DMED(169 images)	97.04	86.39	96.44	97.04	98.81
DRIVE (40 images)	100	60	100	100	100

Table 3.1: Results for Optic disk detection

Method	Messidor	Directdb0	Directdb1	DMED	Drive
[18] Supervised	-	98.50	97.75	-	97.5
[2] Unsupervised	97.80	86.50	86.50	-	97.5
[38] Supervised	-	97.0	96.20	-	100
[10] Supervised and Ensemble	-	97.64	97.79	-	100
Proposed Un-supervised	98.50	96.15	95.51	97.04	100

Table 3.2: Comparison of Detection Rates for OD

Dataset name	Messidor		Direct		DMED	Drive
	First 400	400-800	db0	db1		
Marked images	340/400	343/400	81/130	58/89	145/169	37/40
Proposed Accuracy	97.5	98	95.85	96	96.44	100

Table 3.3: Detection rates for macula on popular datasets

vised technique [10]. In this table '-' signifies that the method did not report result on that particular dataset.

Only those images, where macula position is clearly visible were marked during local data annotation. We show macula detection results on both local [35, 21, 22, 37] and publicly available [13] markings. Macula detection results are presented in Table 3.3. [8] reports detection accuracy of 98.24% on locally marked 1136(out of 1200) images of Messidor and accuracy of 94.38% on Direct-db1. Their accuracy is slightly higher for messidor but lower for Direct-db1 compared to our method.

Our method performs better for OD detection as compared to macula detection, because macula detection is a harder problem and it's result depends upon accurate OD results, as OD position is used to limit it's search space. Qualitative results for some images are also shown in Fig. 3.8.

The interference map is computed on green channel of illumination corrected image after fundus extension (FOV extension). Creating GMP for an image size of  $R \times C$  has computation complexity of  $O(R \times C \times \theta \times N)$ , as we need to perform  $O(\theta \times N)$  image rotation operations. In our work angle range is  $(-7, 7)$ , number of pivot points are 150 and  $R, C$  are number of rows and columns of image respectively. Because of this GMP computations becomes very slow for high resolution images. To speed up computation, all the images were resized to 640 rows while preserving aspect ratio because

candidate selection is relatively unaffected by resolution reduction as GMP suppresses local information and this also permits the use of a fixed set of theta range and pivot points  $N$  values across datasets.

GMP interference map creation takes 2-3 minutes on a unoptimized, single threaded Matlab code running on Ubuntu with 2.1 GHz processor and 4 GB RAM. After computing GMP interference map, rest of the stages takes 2-3 seconds for computing OD and macula center.

### **3.6 Summary**

In this work, we have used the Generalized motion pattern concept from [14] and [23] and modified it for OD and macula detection. We have tested our algorithm on various public datasets and showed that our method performs better than other unsupervised algorithms. Our method does not require much tuning of parameters across datasets. In the current implementation, the bottleneck is in interference map creation. Since this is highly parallelizable, it can be explored in the future.

## *Chapter 4*

### **An effective metric for evaluating retina blood vessel segmentation performance: Local accuracy**

Retina blood vessel structure is an important indicator of various retina related diseases, which has motivated the development of various vessel segmentation algorithms. These algorithms have been evaluated using generic metrics, without any justification of the usefulness and reliability in the task of evaluating retina vessel segmentation performance. In this chapter, we examine the traditional metrics and establish that these evaluation metrics are not ideal. We also propose a new evaluation metric: local accuracy, which is an extension of [39]. Local accuracy calculates accuracy on a subset of retina field of view(FOV) pixels, instead of all pixels. It is robust to imaging changes like change in FOV, change in vessel vs background pixel ratio, while being sensitive to disease specific tissue artifacts like lesions, hemorrhage etc. To validate Local accuracy, we compare the response of various evaluation metrics on common use cases. We also quantitatively compare local accuracy with popular evaluation metrics on 5 public datasets. Current results shows the value of Local accuracy, both as an evaluation metric and as an optimization function.

#### **4.1 Introduction**

Retina blood vessel segmentation is a fundamental task, as vessels are important landmark in retina images and changes in retinal vessel structure are indicator of various disease. Retina diseases effects the structure of blood vessels, so analysis of accurately segmented vessels can help in automated disease diagnosis. In diabetic retinopathy, the pressure in blood vessel increases, which leads to formation of micro-aneurysms and hemorrhages [27]. Similarly, in hypertension, changes in vessel tortuosity, caliber and branching angle occurs. Retina vessel segmentation helps in diagnosis of many other diseases ex. ROP(retinopathy of prematurity), arteriolar narrowing, cardiovascular disease etc. Accurate vessel segmentation also helps in rejecting false positives in micro-aneurysm & hemorrhage detection [24].

Since retina vessel segmentation is an important problem, the thorough validation of segmented vessels is also an important task. Thorough validation can increase the confidence in a specific method

and can be a decisive factor to use it. A plethora of possibilities exists to analyze the performance of an algorithm and in the past, community has been using generic image similarity measures like sensitivity, specificity, accuracy, positive prediction rate, negative prediction rate and area under receiver operating characteristic (AUC). Recently, there has been some efforts to define retina specific evaluation methods. [29] modifies  $F_1$  measures to capture subtle changes in branching and bifurcation angle and [39] propose Local accuracy. In this chapter, we extend the local accuracy idea to make it more robust and reasonable.

In retina images, the vessel vs background pixel ratio is low, as there are lot more background pixels compared to vessel pixels. Every work in literature calculates the performance metrics on all pixels in retina FOV. Due to significant difference in vessel vs background pixel ratio, segmentation methods end up becoming biased towards background during parameter tuning and mis-classify weak vessels as background. The traditional approaches are also less discriminative, very sensitivity to change in FOV and less sensitive to disease specific tissue artifacts like lesions, hemorrhage etc.

To overcome these issues, we propose a new metric for evaluating retina blood vessel segmentation performance: Local accuracy. In local accuracy, we calculate accuracy on a subset of pixels instead of whole retina FOV. These subset of pixels are combination of neighboring pixels around true vessels and false positives detected by segmentation algorithm. In the results section, we will theorize an ideal performance metric by defining its behavior in various retina use cases. We show the value of local accuracy by showing that local accuracy is very close to ideal performance metric.

Rest of the paper is organized as follows: Section 4.2 gives an literature overview. Section 4.3 explains the local accuracy in details. Section 4.4 lists the experiments done and report quantitative and qualitative results. Conclusion is given in Section 4.5.

## 4.2 Related works

In this section, we summarize popular metrics used in literature for evaluating retina vessel segmentation performance. Suppose for a given retina image  $I$ ,  $V_{seg}$  and  $V_{gt}$  are 2 binary images representing the segmented vessel tree and marked ground truth. Each pixel of these binary images can take 2 values: 1 or 0, here 1 represents vessel pixels and 0 represents background pixels. Value of 1 in  $V_{seg}$  means that the segmentation algorithm has detected this location as vessel. Similarity 1 value of  $V_{gt}$  means that the annotator has marked this location as a vessel. Given these 2 binary images, all the pixels in FOV of  $I$  can be divided into 4 subsets: True positives ( $TP$ ), False positives ( $FP$ ), True Negatives ( $TN$ ) and False Negatives ( $FN$ ).  $TP$  and  $TN$  are the number of vessel and background pixels which are correctly detected.  $FP$  is the number of background pixels which are mis-classified as vessels and  $FN$  is the number of vessel pixels which are mis-classified as background. The most popular evaluation metrics are defined as:

$$Accuracy = \frac{TP + TN}{TP + TN + FP + FN} \quad (4.1)$$

$$Sensitivity = \frac{TP}{TP + FN} \quad (4.2)$$

$$Specificity = \frac{TN}{TN + FP} \quad (4.3)$$

The value of all 3 metrics varies between 0 and 1. Sensitivity represents the amount of vessels, which are correctly classified by algorithm and it doesn't care about background pixels. Similarly, specificity represents the amount of background pixels, which are correctly classified. Accuracy captures both vessel and background and accuracy value of 1 means that every pixel is classified correctly. Some other less popular metrics are: Positive Prediction Value ( $Ppv$ ), Negative Prediction Value ( $Npv$ ), Matthews Correlation Coefficient ( $MCC$ ) and Area Under Receiving Operator Characteristics Curve ( $AUC$ ). These metrics are defined as:

$$Ppv = \frac{TP}{TP + FP} \quad (4.4)$$

$$Npv = \frac{TN}{TN + FN} \quad (4.5)$$

$$MCC = \frac{TP \times TN - FP \times FN}{(TP + FP)(TP + FN)(TN + FP)(TN + FN)} \quad (4.6)$$

$Ppv$  and  $Npv$  represents the purity of vessels and background respectively. Their value ranges from 0 to 1.  $MCC$  is the correlation between segmented vessel tree and ground truth and its value varies between -1 and 1.  $MCC$  value of 1,0 and -1 means perfect correlation (perfect prediction), no correlation (random prediction) and negative correlation (completely incorrect prediction) respectively. Receiving operator characteristics (ROC) curve is a plot of sensitivity versus (1 - specificity). ROC curve is obtained by varying the detection threshold in its range. The closer the ROC curve gets to top left corner, the better our prediction system is.  $AUC$  is area under ROC curve. Its value is 1 for a system, which does perfect prediction for all detection threshold values.

Above metrics are designed and used to quantify generic binary classifications but they are not ideal for evaluating blood vessel segmentation performance. Retina blood vessel segmentation literature uses above metrics on all pixels in retina FOV to calculate performance numbers. We will refer to these metrics as global metrics because they use all pixels in retina FOV. Global metrics are less discriminative, very sensitivity to change in FOV and less sensitive to disease specific tissue artifacts like lesions, hemorrhage etc. In next section, we will define a new evaluation metric: Local Accuracy and in experiment section we will explain how Local Accuracy overcome these problems, while fulfilling field specific requirements.

### 4.3 Local accuracy

The idea of local accuracy is to use subset of pixels, instead of all pixels in retina field of view(FOV) for evaluating segmentation performance. Local accuracy was first proposed in [39], where they dilated the manual vessel markings to get neighboring pixels. They calculated sensitivity, specificity and

accuracy on neighboring pixels and called it local sensitivity, local specificity and local accuracy respectively. There are some flaws with choosing neighboring pixels using simple dilation, which we have listed below.

1. The dilation approach does not penalize all false positives, as it only considers pixels on and around manual vessel markings in calculation. If lesions, microaneurysm, imaging noise etc. are getting falsely detected as vessels and they are not within the dilated neighborhood, it does not penalize them.
2. The number of neighboring pixels around both strong and weak vessels are same but neighboring pixels should be proportional to vessel width. We would want more neighboring pixels around strong vessels and fewer neighboring pixels around weak vessel.
3. The choice and size of dilation operator needs to be specified manually for each dataset. The original work [39] reported results for structuring elements of varying size on same dataset.

In this work, we have modified the definition of neighboring pixels to address above issues and explained it below. We initiate the structuring element( $SE$ ) as  $3 \times 3$  square and the neighborhood pixels image( $I_{neighbors}$ ) as zero image. Let's call manually marked vessel image as  $I_{vess}$  and output of segmentation algorithm as  $I_{seg}$ . To compute neighborhood pixels image, we compute a new image  $I_{in}$ , which has value 1 for all the pixels where either  $I_{vess}$  or  $I_{seg}$  is 1 and 0 elsewhere.  $I_{in}$  contains both marked vessels and false positives(FP) detected by segmentation algorithm. Given image  $I_{in}$ , we calculate ( $I_{neighbors}$ ) as follows:

1. Apply morphological opening operation on  $I_{in}$  using  $SE$ , vessels and FP which are thinner than  $SE$  will disappear in morphological opened  $I_{in}$ .
2. Calculate the difference between  $I_{in}$  and  $I_{in}$  after opening, this difference image will only have thin vessels and thin FP, which were removed in step 1 due to opening.
3. Apply morphological dilation with  $SE$  on difference image from last step. Pixels in dilated difference image represents the neighborhood of removed thin vessels and FP. We add dilated difference image in  $I_{neighbors}$ .
4. Update  $I_{in}$  by applying morphological opening operation. We want to permanently remove vessels and FP, for which neighborhood is calculated and added in  $I_{neighbors}$ .
5. Increase the size of  $SE$ .
6. Repeat step 1-5 until there are no pixels in  $I_{in}$ . This happens when  $SE$  is bigger then even the thickest structure in  $I_{in}$ .

The final image contains neighboring pixels around both vessel markings and falsely detected vessels. We use pixels in ( $I_{neighbors}$ ) to calculate local sensitivity, local specificity and local accuracy. Figure 4.1 shows some examples images of calculated neighboring pixels.

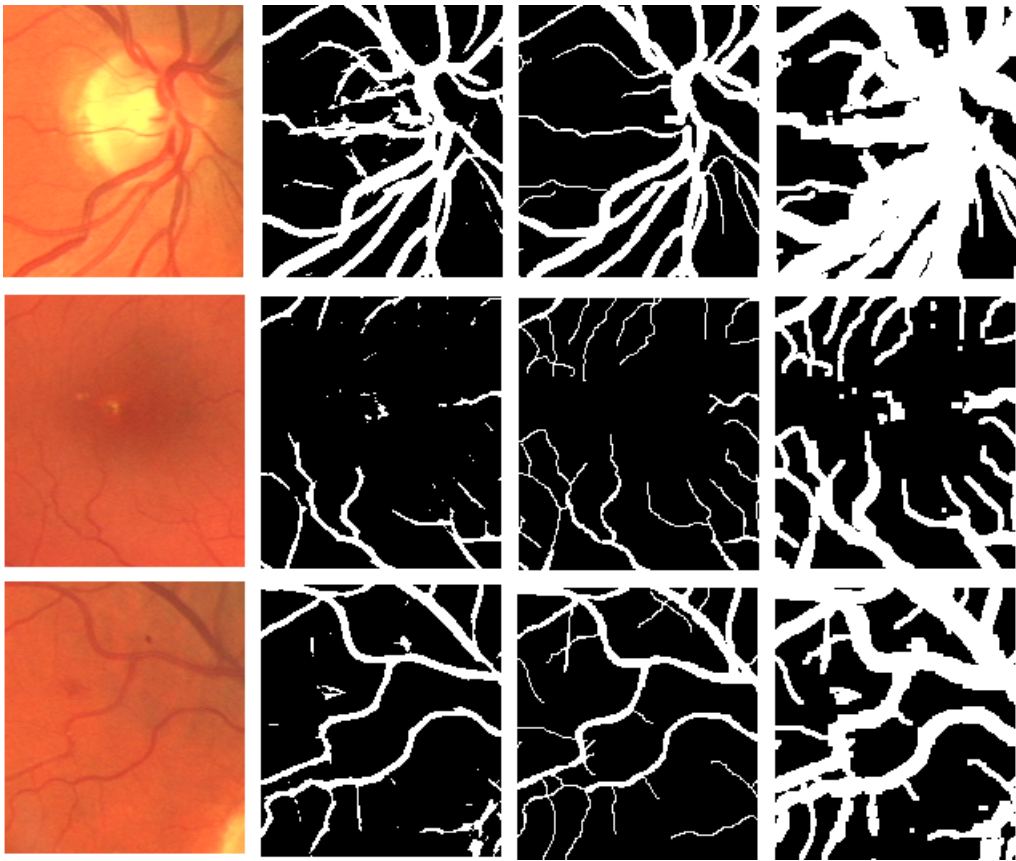


Figure 4.1: From left to right a) Original image b) Segmented vessels using [31] c) Manually marked vessels d) Neighborhood pixels .

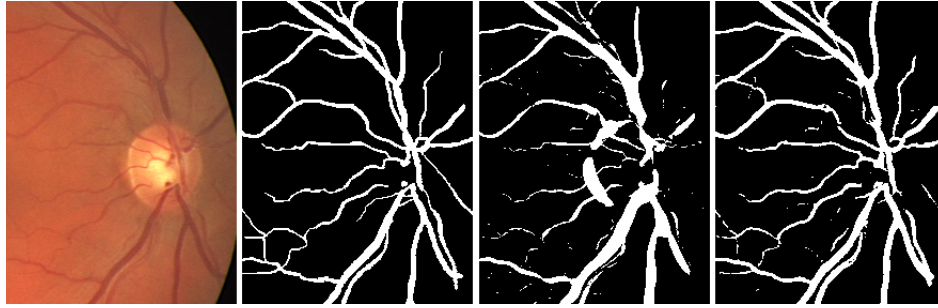


Figure 4.2: From left to right a) Original image b) Manually marked vessels c) Segmented vessels using [25] d) Segmented vessels using [28] .

## 4.4 Results and experiments

To validate the local accuracy, we have discussed common retina use cases and response of different evaluation metrics in said use cases. Accuracy, sensitivity and specificity are most commonly used global evaluation metrics and we will be using them for comparison. We will then theorize an ideal evaluation metric and show that local accuracy is very near to ideal evaluation metric.

### 4.4.1 Discriminative power

Discriminative power represents the evaluation metric's ability to differentiate between competing methods and its ability to quantify good or bad segmentation. Most retina vessel segmentation methods scores close quantitative results on popular datasets using global evaluation metrics. This is because most methods detect background correctly, which means very high number of TN and this results in high accuracy. An ideal evaluation metric should have high discriminative power to get a true sense of segmentation performance. Fig. 4.2 shows a sample image and its segmentation by a popular (but relatively old) hessian based method [25] and recent state of the art deep learning based method [28]. As seen in Fig. 4.2, the difference in segmentation results is huge but the segmentation accuracy is very close. The segmentation accuracy for [25] and [28] are 0.927 and 0.955 respectively, while local accuracy for [25] and [28] are 0.777 and 0.895 respectively for the same segmentation.

### 4.4.2 Effect of change in FOV

Retina field of view(FOV) indicates the portion of retina we are capturing. In low FOV setting, we are capturing relatively small central part of retina and the area near OD is zoomed in. In low FOV, the vessel vs background pixel ratio is high, as the retina vessels are most dense around OD region. Similarly, in higher FOV, the vessel vs background pixel ratio is low. Accuracy and specificity are very sensitive to vessel vs background pixel ratio as background pixels are correctly detected by most



Figure 4.3: From left to right a) Drive image b) Stare image

segmentation methods. Change in vessel vs background pixel ratio means change in True negative count, which directly affects accuracy and specificity calculation. Since accuracy and specificity are very sensitive to vessel vs background ratio, they are also very sensitive to change in retina FOV. Ideal metric shouldn't be sensitive to change in FOV because small change in FOV doesn't change anything other than scale of structure. Local accuracy is not sensitive to change in FOV because we only consider pixels around marked vessels and false positives instead of all pixels in retina FOV, while calculating performance numbers. To quantitatively prove this, we took most similar looking healthy eye image pair from drive and stare. Drive dataset has 45 degree FOV and stare has 35 degree FOV. We compared [28] segmentation results on both images and evaluation number are substantially different for global evaluation metrics compared to local evaluation metrics. Accuracies for chosen Drive and Stare images are 0.966 and 0.943 respectively, while the local accuracies for Drive and Stare for the same segmentation are 0.848 and 0.845.

#### 4.4.3 Penalizing mis-detection due to lesions and other abnormalities

During vessel segmentation, sometimes non-vessel gets detected as vessels(false positives). These false positives are present due to

1. **Clinical reasons and retina diseases:** Even in healthy eyes, there are subtle differences in background because of non-uniformity of tissue layers. These changes in background can be mis-detected as vessels. In abnormal eyes, lesions, micro-aneurysm, hemorrhage etc. are present due to diseases like Diabetic retinopathy, glaucoma etc. These diseases effect segmentation performance as these lesions and hemorrhages are usually misdetected as vessels. Basically, these false positives are present because of non-vessel but similar looking signal present in tissue layer.

2. **Imaging conditions:** Segmentation accuracy is directly proportional to imaging quality. Non-uniform intensities, imaging noise, bad focus, low signal etc. have direct impact on segmentation performance. Pre-processing is often used to deal with bad imaging conditions and improve signal to noise ratio in retina images. Artifacts due to imaging conditions are often detected as vessels.

The number of false positives are very low (pixel count wise) due to retina diseases and other clinical reasons. This is because micro-aneurysm, lesions etc. are very small structure. Their mis-detection is not properly captured in global evaluation metrics.

Bad imaging condition usually causes mis-detection of higher pixels and thus it has much more effect on global evaluation metrics. An ideal evaluation method should be highly sensitive to mis-classification by clinical and disease specific abnormalities and sensitive to mis-classification cause by bad imaging. Local accuracy is highly sensitive to both mis-classifications as we use pixels near false positive as a part of our neighboring pixels.

#### 4.4.4 Local accuracy as an optimization method

Most vessel segmentation methods segment vessels as a vesselness image. Vesselness image is a gray scale image with multiple intensity levels. The intensity value in vesselness image represents it's probability of being true vessel and this vesselness image is thresholded to get binary segmentation. The threshold is optimized to achieve highest quantitative performance and in literature accuracy has been the default choice of evaluation metric for optimizing quantitative results. Due to the reasons discussed above, results optimized using accuracy ends up ignoring weak vessels. In this section, we optimize results using local accuracy and compare them with the results generated using optimizing accuracy. We show that local accuracy detects weak vessels better but it also creates little more false positives.

Table 4.1 gives accuracies and local accuracies for popular segmentation methods on Drive [13] dataset and the threshold is optimized to maximize accuracy. Table 4.2 gives accuracies and local accuracies for same methods and dataset but the threshold is optimized to maximize local accuracy.

Some observation that we can make from quantitative results are:

1. Sensitivity is higher when we optimize to maximize local accuracy. This is because we are removing background bias cause by low vessel vs background pixel ratio.
2. Local accuracy is more discriminative as the performance numbers are further apart in case of local accuracy. If you see the quantitative numbers, the number range is much higher for local accuracy.

In order to show visual difference in results using accuracy and local accuracy, we have shown example image from Drive dataset which is segmented using multi-scale line detector [39]. Fig. 4.4 shows image patch, manual marking, segmentation optimized for accuracy and segmentation optimized for local accuracy. As we can see, local accuracy version segments more weak vessels.

Segmentation method and evaluation metric	Sensitivity	Specifity	Accuracy	Local sensitiv-ity	Local specificity	Local ac-curacy
Hassian based - 1998 [25]	0.61	0.973	0.927	0.61	0.888	0.78
Wavelets - 2006 [33]	0.712	0.973	0.94	0.712	0.884	0.816
Line Detectors - 2007 [7]	0.514	0.981	0.921	0.514	0.925	0.748
Kernel Boost - 2013 [4]	0.722	0.98	0.947	0.722	0.91	0.834
Multi scale line detectors - 2013 [39]	0.687	0.981	0.943	0.687	0.913	0.823
N4 fields - 2014 [40]	0.763	0.979	0.951	0.763	0.905	0.846
Holistically-nested edge detection - 2015 [36]	0.734	0.981	0.949	0.734	0.911	0.838
Structured Forests - 2015 [32]	0.532	0.978	0.921	0.532	0.902	0.753
Deep retinal image under-standing - 2016 [28]	0.793	0.979	0.955	0.793	0.905	0.859

Table 4.1: Accuracies and local accuracies for Drive [13] dataset. Threshold optimized for maximizing accuracy.

Segmentation method and evaluation metric	Sensitivity	Specifity	Accuracy	Local sensitiv-ity	Local specificity	Local ac-curacy
Hassian based - 1998 [25]	0.701	0.954	0.922	0.701	0.838	0.789
Wavelets - 2006 [33]	0.758	0.965	0.939	0.758	0.857	0.818
Line Detectors - 2007 [7]	0.592	0.96	0.913	0.592	0.888	0.754
Kernel Boost - 2013 [4]	0.754	0.974	0.946	0.754	0.89	0.836
Multi scale line detectors - 2013 [39]	0.743	0.97	0.941	0.743	0.879	0.827
N4 fields - 2014 [40]	0.8	0.972	0.95	0.8	0.881	0.848
Holistically-nested edge detection - 2015 [36]	0.782	0.973	0.948	0.782	0.882	0.842
Structured Forests - 2015 [32]	0.616	0.961	0.917	0.616	0.848	0.76
Deep retinal image under-standing - 2016 [28]	0.82	0.974	0.954	0.82	0.888	0.86

Table 4.2: Accuracies and local accuracies for Drive [13] dataset. Threshold optimized for maximizing local accuracy.

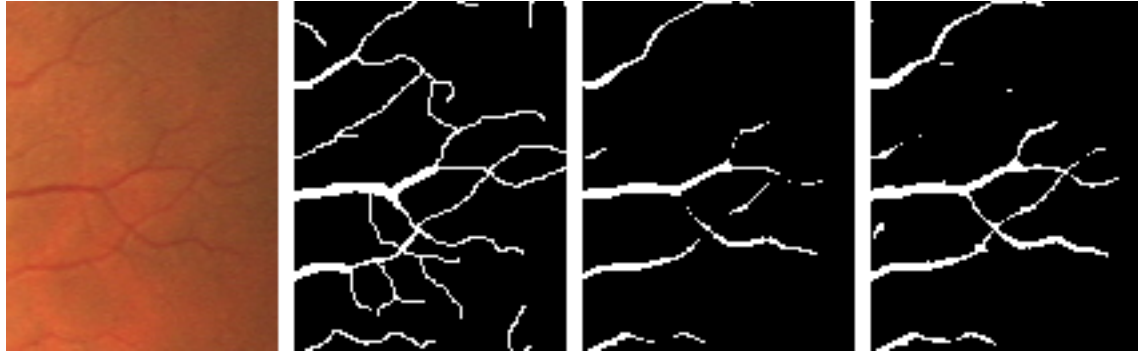


Figure 4.4: From left to right a) Original image b) Manually marked vessels c) Segmented using [39] and optimized for accuracy d) Optimized for Local accuracy.

Segmentation method and evaluation metric	Sensitivity	Specifity	Accuracy	Local sensitiv-ity	Local specifity	Local ac-curacy
Deep retinal image understanding [28]	0.796	0.985	0.965	0.796	0.909	0.862
Hassian based [25]	0.543	0.978	0.935	0.543	0.895	0.747
Holistically-nested edge detection [36]	0.757	0.982	0.96	0.757	0.901	0.841
Line Detectors [7]	0.613	0.985	0.948	0.613	0.921	0.79
Multi scale line detectors [39]	0.718	0.98	0.952	0.718	0.886	0.819
Wavelets [33]	0.74	0.98	0.954	0.74	0.884	0.826
BCOSFIRE [3]	0.735	0.977	0.952	0.735	0.875	0.819

Table 4.3: Accuracies and local accuracies for Stare [26] dataset. Threshold optimized for maximizing accuracy.

Segmentation method and evaluation metric	Sensitivity	Specifity	Accuracy	Local sensitiv-ity	Local specificity	Local ac-curacy
Deep retinal image understanding [28]	0.829	0.981	0.965	0.829	0.888	0.864
Hassian based [25]	0.703	0.952	0.928	0.703	0.811	0.766
Holistically-nested edge detection [36]	0.81	0.975	0.959	0.81	0.868	0.844
Line Detectors [7]	0.708	0.969	0.943	0.708	0.869	0.799
Multi scale line detectors [39]	0.781	0.97	0.95	0.781	0.85	0.823
Wavelets [33]	0.776	0.975	0.953	0.776	0.863	0.828
BCOSFIRE [3]	0.795	0.968	0.95	0.795	0.844	0.825

Table 4.4: Accuracies and local accuracies for Stare [26] dataset. Threshold optimized for maximizing local accuracy.

Evaluation metrics	Sensitivity	Specifity	Accuracy	Initial local ac-curacy	Proposed local accuracy	Ideal
Discriminative power	<b>High</b>	Low	Low	<b>High</b>	<b>High</b>	High
Robustness to change in FOV	<b>High</b>	Low	Low	<b>High</b>	<b>High</b>	High
Sensitivity to lesions and other abnormalities	Zero	Medium	Medium	Zero	<b>High</b>	High
Penalty for false positives	Zero	Medium	Medium	Zero	<b>High</b>	High

Table 4.5: Comparison of different evaluation metrics.

## 4.5 Summary

In this work, we have proposed an effective metric for evaluating retina blood vessel segmentation performance. Our work is an extension of [39]. Results and experiments done using public datasets shows the value of proposed evaluation metric. We have summarized the comparison results in Table 4.5. We hope that in future retina community will start reporting segmentation results using our metric along with traditional metrics.

## *Chapter 5*

### **Conclusions**

Assisted diagnosis and automated analysis are need of the hour to improve diagnosis time, diagnosis accuracy and affordabability. This work is an another step in the journey of automated analysis of human retina images. Retina research community has been developing tools and systems to help doctor make the final diagnosis for quite some time but recent years has seen spark in such activities because of increase in computation power and availability of more public data. In retina images, there are some important landmarks and all automated analysis systems needs the location of above landmarks for detection and diagnosis.

In this work, we explored retina atlas with the focus of finding their application in OD and macula detection. We marked a lot of data manually for this work and defined intensity and probability atlases. The algorithm is supervised but it also needs vessel arcade information along with OD and location for training, which is a downside of our algorithm. The results are satisfactory but simpler approaches outperform our detection accuracies, so it's not very practical. To improve detection accuracies, we have used the Generalized motion pattern concept from [14] and [23] and modified it for OD and macula detection. Our GMP based method performs better than other unsupervised algorithms.

In last chapter, we have proposed an effective metric for evaluating retina blood vessel segmentation performance. Our work is an extension of [39]. Results and experiments done using public datasets show the value of proposed evaluation metric. We hope that in future retina community will start reporing segmentation results using our metric along with traditional metrics.

## **Related Publications**

1. G. Mittal and J. Sivaswamy, “Optic disk and macula detection from retinal images using Generalized Motion Pattern” 2015 Fifth National Conference on Computer Vision, Pattern Recognition, Image Processing and Graphics (NCVPRIPG), Patna, 2015, pp. 1-4. doi: 10.1109/NCVPRIPG.2015.7490071

## Bibliography

- [1] Sharib Ali, Dsir Sidib, Kedir M. Adal, Luca Giancardo, Edward Chaum, Thomas P. Karnowski, and Fabrice Mriaudeau. Statistical atlas based exudate segmentation. *Computerized Medical Imaging and Graphics*, pages 358–368, 2013.
- [2] M. I. Ahmed et al. High speed detection of optical disc in retinal fundus image. *Signal, Image and Video Processing*, pages 77–85, 2015.
- [3] George Azzopardi. Trainable COSFIRE filters for vessel delineation with application to retinal images. *Medical image analysis 19.1*, pages 46–57, 2015.
- [4] C. Becker, R. Rigamonti, V. Lepetit, and P. Fua. Supervised feature learning for curvilinear structure segmentation. *Medical Image Computing and Computer-Assisted Intervention(MICCAI)*, pages 526–533, 2013.
- [5] F.L. Bookstein. Principal Warps: Thin-Plate Splines and the Decomposition of Deformations. *PAMI*, pages 567–585, 1989.
- [6] chasedb1 release team. Kindly provided by the retinal image analysis group of Kingston University London (see <https://blogs.kingston.ac.uk/retinal>).
- [7] Ricci Elisa and Renzo Perfetti. Retinal blood vessel segmentation using line operators and support vector classification. *IEEE Transactions on Medical Imaging*, pages 1357–1365, 2007.
- [8] A. Aquino et al. Establishing the macular grading grid by means of fovea centre detection using anatomical-based and visual-based features. *Computers in Biology and Medicine, Science direct*, 2014.
- [9] A. D Fleming et al. Automated Assessment of Diabetic Retinal Image Quality Based on Clarity and Field Definition. *Investigative Ophthalmology and Visual Science*, pages 1120–1125, 2006.
- [10] A Giachetti et al. Combining algorithms for automatic detection of optic disc and macula in fundus images. *Computer Vision and Image Understanding*, pages 138–145, 2012.
- [11] Aliaa Abdel Haleim et al. Optic disc detection from normalized digital fundus images by means of a vessels direction matched filter. *IEEE Transactions on Medical Imaging*, 2008.

- [12] H. Li et al. Automatic location of optic disk in retinal images. *International conf on image processing*, pages 837–840, 2001.
- [13] J.J. Staal et al. Ridge based vessel segmentation in color images of the retina. *IEEE Transactions on Medical Imaging*, 2004.
- [14] K. Sai Deepak et al. Automatic Assessment of Macular Edema From Color Retinal Images. *IEEE Transactions on medical imaging*, 2012.
- [15] M. E. Gegundez-Arias et al. Locating the fovea center position in digital fundus images using thresholding and feature extraction techniques. *Computerized Medical Imaging and Graphics*, pages 386–393, 2013.
- [16] M. N. Michael et al. Fast detection of the optic disc and fovea in color fundus photographs. *Medical image analysis*, pages 859–870, 2009.
- [17] R.J. Qureshi et al. Combining algorithms for automatic detection of optic disc and macula in fundus images. *Computer Vision and Image Understanding*, 116.1:138–145, 2012.
- [18] S. A. Ramakanth et al. OD-Match: patchmatch based optic disk detection. *Fourth National Conference NCVPRIPG*, pages 1–4, 2013.
- [19] S. Lu et al. Automatic optic disc detection from retinal images by a line operator. *IEEE Transactions on Biomedical Engineering*, 2011.
- [20] S. S. Waleed et al. Automated localisation of retinal optic disk using hough transform. *Biomedical Imaging: From Nano to Macro, IEEE ISBI*, 2008.
- [21] T. Kauppi et al. DIARETDB0: Evaluation database and methodology for diabetic retinopathy algos. *Machine Vision and Pattern Recognition Research Group, Lappeenranta University of Technology*, 2006.
- [22] T. Kauppi et al. The DIARETDB1 Diabetic Retinopathy Database and Evaluation Protocol. *British Machine Vision Conference*, 2007.
- [23] Ujjwal et al. An assistive annotation system for retinal images. *IEEE International Symposium on Biomedical Imaging*, 2015.
- [24] Oliver Faust, Rajendra Acharya, E. Y. K. Ng, Kwan-Hoong Ng, and Jasjit S. Suri. Algorithms for the automated detection of diabetic retinopathy using digital fundus images: a review. *Journal of medical systems*, pages 145–157, 2012.
- [25] A F Frangi. Multiscale vessel enhancement filtering. *Medical Image Computing and Computer-Assisted Intervention MICCAI*, pages 130–137, 1998.

- [26] A. Hoover and other stare resease team. Kindly provided by the retinal image analysis group of Clemson University, South Calorina (see <http://cecas.clemson.edu/~ahoover/stare/>).
- [27] Nicky Lai. Clinical ophthalmology: A systematic approach. *Optometry and Vision Science*, page 295, 2004.
- [28] Kevis-Kokitsi Maninis, Jordi Pont-Tuset, Pablo Arbelaez, and Luc Van Gool. Deep retinal image understanding. *International Conference on Medical Image Computing and Computer-Assisted Intervention*, pages 140–148, 2016.
- [29] Uyen T V Nguyen, Laurence A F Park, Liang Wang, and Alauddin Bhuiyan. A quantitative measure for retinal blood vessel segmentation evaluation. *International Journal of Computer Vision Signal Processing*, pages 1–8, 2012.
- [30] Rajendra Acharya et al. Oliver Faust. Algorithms for the Automated Detection of Diabetic Retinopathy Using Digital Fundus Images: A Review. *Journal of Medical Systems*, 36:145–157, 2012.
- [31] J.I. Orlando and M. Blaschko. Learning Fully-Connected CRFs for Blood Vessel Segmentation in Retinal Images. *Medical Image Computing and Computer-Assisted Intervention MICCAI*, 2014.
- [32] Dollr Piotr and C. Lawrence Zitnick. Fast edge detection using structured forests. *IEEE transactions on pattern analysis and machine intelligence*, pages 1558–1570, 2015.
- [33] Ghaderi R, Hassanpour H, and Shahiri M. Retinal vessel segmentation using the 2-D Morlet wavelet and neural network. *International Conference on Intelligent and Advanced Systems*, pages 1251–1255, 2007.
- [34] Jones Allan R., Caroline C. Overly, and Susan M. Sunkin. The Allen brain atlas: 5 years and beyond. *Nature Reviews Neuroscience 10.11*, pages 821–828, 2009.
- [35] Messidor release team. Kindly provided by the messidor program partners (see <http://messidor.crihan.fr>).
- [36] Xie Saining and Zhuowen Tu. Holistically-nested edge detection. *IEEE international conference on computer vision*, pages 1395–1403, 2015.
- [37] DMED team. Kindly provided by the DMED program partners (see <http://vibot.u-bourgogne.fr/luca/heimed.php>).
- [38] A. Tewari and J. Sivaswamy. Bilateral Symmetry Based Approach for Joint Detection of Landmarks in Retinal Images. *International Conference on Singnal Processing and Communications*, 2014.

- [39] Uyen T.V.Nguyen, Alauddin Bhuiyan, Laurence A. F. Park, and Kotagiri Ramamohanarao. An effective retinal blood vessel segmentation method using multi-scale line detection. *Science direct Pattern recognition*, pages 703–715, 2013.
- [40] Ganin Yaroslav and Victor Lempitsky. N4-fields: Neural network nearest neighbor fields for image transforms. *Asian Conference on Computer Vision(ACCV)*, pages 536–551, 2014.